Angewandte Chemie
Eine Zeitschrift der Gesellschaft Deutscher Chemiker

Supporting Information

Calcium-Ion Binding Mediates the Reversible Interconversion of *Cis* and *Trans* Peroxido Dicopper Cores

*Natasha P. Vargo, Jill B. Harland, Bradley W. Musselman, Nicolai Lehnert,**
Mehmed Z. Ertem, and Jerome R. Robinson**

ange_202105421_sm_miscellaneous_information.pdf
ange_202105421_sm_Structures.xyz

Supporting Information

Table of contents

1. General synthetic methods and materials

Unless specified, all reactions were performed under inert atmosphere (N_2) using standard Schlenk techniques or in a MBraun glovebox equipped with a standard catalyst purifier and solvent trap (< 0.1 ppm O_2 and H_2O), and all reagents and solvents were stored long-term in an N_2-filled glovebox. In the case of $^{16}O_2$ reactions, these were performed using standard Schlenk technique (see Section 1.3. for $^{18}O_2$ procedure). Glassware was oven-dried for at least 2 h at 150 °C prior to use. Celite and 3 Å molecular sieves were heated at 300 °C under reduced pressure (~100 mTorr) for at least 24 h cooled, and then brought into an N_2-filled glovebox for use. Specific details regarding instrumentation are described in their respective sections.

1.1. Materials

HPLC-grade tetrahydrofuran (inhibitor-free), diethyl ether (inhibitor-free), acetonitrile and toluene, were purchased from Fisher Scientific. Solvents were sparged for 20 min with dry argon and dried using a commercial two-column solvent purification system (LC Technologies). These solvents were further dried by storing them over 3 Å molecular sieves for at least 48 h prior to use. Acetone (99.8%, Acros, Extra Dry AcroSeal®) was used without further purification. d_6-Acetone was stirred over B_2O_3 for 24 h, vacuum transferred, degassed (freeze-pump-thaw), and stored in an N_2-filled glovebox. Propionitrile (99%, Acros) was degassed (freeze-pump-thaw) and stored over 3 Å molecular sieves in N_2-filled glovebox. Distilled deionized water (ddH_2O) was used for all syntheses and experiments.

Tetrakis(acetonitrile)copper(I) hexafluorophosphate ($[Cu^I(CH_3CN)_4][PF_6]$, 98+%, Strem Chemicals), copper(II) perchlorate hexahydrate ($[Cu^{II}(ClO_4)_2]\cdot 6H_2O$], 98+%, Strem Chemicals), Calcium perchlorate ($Ca(ClO_4)_2$ anhydrous, 99%, Sigma-Aldrich), tetrabutylammonium hydroxide ($[NBu_4][OH]$,1 M solution in MeOH, Acros), trifluoromethanesulfonic acid (HOTf, 99.5%, Oakwood), Cobaltocene ($CoCp_2$, > 99%, Strem Chemicals), $^{16}O_2$ (99.6%, AirGas), and $^{18}O_2$ (99%, Sigma-Aldrich) were used as received. Calcium triflate ($Ca(OTf)_2$, 99%, Oakwood) was dried under reduced pressure (100 °C, 10 mTorr, 12 h) prior to use. 18-crown-6 (≥ 99%, Chem-Impex International) was purified by recrystallization in anhydrous acetonitrile under inert-atmosphere and dried under reduced pressure (80 °C, 10 mTorr, 24 h) to furnish anhydrous material.[1] Tris(2-pyridylmethyl)-amine (TMPA),[2] $[Cu^ITMPA(CH_3CN)][PF_6]$ (**$[Cu^I]^+$**),[3] $[Cu^{II}TMPA(CH_3CN)][ClO_4]_2$ (**$[Cu^{II}]^{2+}$**),[4] and $\{[Cu(TMPA)]_2(\mu\text{-}1,2\text{-}O_2^{2-})\}^{2+}$ **(1)**,[3, 5] were synthesized according to literature procedures.

1.2. Synthesis of tetrabutylammonium triflate, $[NBu_4][OTf]$.

A 250 mL round-bottomed flask was charged with tetrabutylammonium hydroxide ($[NBu_4][OH]$, 19.27 mL, 19.27 mmol, 1 M in MeOH; MW: 259.48 g·mol^{-1}), H_2O:MeOH (60 mL; 9:1 V/V), and a Teflon-coated stir-bar. Trifluoromethanesulfonic acid (HOTf, 1.7 mL, 2.89 g, 19.27 mmol, 1 equiv; MW: 150.07 g·mol^{-1}) was added dropwise at RT to the colorless solution using a volume-calibrated glass Pasteur pipette (*Caution*: HOTf is extremely corrosive and will fume upon exposure to air. This should be handled in a properly ventilated fume hood at all times). The clear, light-yellow solution was stirred overnight. Dichloromethane (100 mL) was added to the solution and stirred for 1 hour. The organic layer was then separated, washed with water (3 x 50 mL), dried with Na_2SO_4, filtered, and solvents were removed under reduced pressure. The resulting crude light-yellow oil was triturated with diethyl ether (200 mL) to yield an off-white powdery solid. This powder was dried under reduced pressure (100 °C, 10 mTorr; 24 h) to yield anhydrous tetrabutylammonium triflate, $[\mathrm{NBu_4}][\mathrm{OTf}]$, as a white solid. Yield: 7.53 g (19.2 mmol, 99%; MW: 391.53 $\mathrm{g{\cdot}mol^{-1}}$). Spectral data matched those previously reported (Figure S23).[6]

^{1}H NMR (600 MHz, $\mathrm{CDCl_3}$, 298 K): δ 0.68 (t, ^3J = 7.4 Hz, 3H, $\mathrm{N(CH_2CH_2CH_2C\underline{\mathit{H}_3})^+}$), 1.10 (sx, ^3J = 7.5 Hz, 2H, $\mathrm{N(CH_2CH_2C\underline{\mathit{H}_2}CH_3)^+}$), 1.32 (p, ^3J = 8.0 Hz, 2H, $\mathrm{N(CH_2C\underline{\mathit{H}_2}CH_2CH_3)^+}$), 2.91 (t, ^3J = 8.6 Hz, 2H, $\mathrm{N(CH_2C\underline{\mathit{H}_2}CH_2CH_3)^+}$). ^{13}C NMR (152 MHz, $\mathrm{CDCl_3}$, 298 K): δ 12.76 ($\mathrm{N(CH_2CH_2CH_2\underline{\mathit{C}}H_3)^+}$), 18.83 ($\mathrm{N(CH_2CH_2\underline{\mathit{C}}H_2CH_3)^+}$), 23.08 ($\mathrm{N(CH_2\underline{\mathit{C}}H_2CH_2CH_3)^+}$), 57.86 ($\mathrm{N(\underline{\mathit{C}}H_2CH_2CH_2CH_3)^+}$), 120.32 (q, $\mathrm{\underline{\mathit{C}}F_3SO_3^-}$). ^{19}F-NMR (564.5 MHz, $\mathrm{CDCl_3}$, 298 K): -78.48 ($\mathrm{C\underline{\mathit{F}_3}SO_3^-}$).

1.3. $^{18}O_2$ gas set-up and procedure

An $^{18}\mathrm{O_2}$ gas cylinder was fitted with a Swagelok® adapter fitted with ¼” O.D. stainless steel tubing to a three-way ball valve. The three-way valve was connected to the $^{18}\mathrm{O_2}$ gas cylinder, tubing to a Schlenk line, and Tygon tubing (1/4” O.D.; ~6” in length) capped with a secured, unpierced septa that was replaced after every use (Figure S1). Air was removed from the system through three consecutive evacuation-refill ($\mathrm{N_2}$) cycles employing standard Schlenk technique. The system was placed under static vacuum and $^{18}\mathrm{O_2}$ was delivered to the Tygon tubing. The desired volume of $^{18}\mathrm{O_2}$ gas was then collected with a gas-tight syringe fitted with a stainless steel needle.

Figure S1. $^{18}\mathrm{O_2}$ cylinder Schlenk-line set-up used to minimize air exposure.

2. General Procedures to Synthesize $\{[Cu(TMPA)]_2(\mu\text{-}\eta^1\text{: }\eta^1\text{: }\eta^2\text{-}O_2)[Ca(OTf)]\}^{3+}$ (2)

The title compound, $\{[Cu^{II}(TMPA)]_2(\mu\text{-}\eta^1\text{:}\eta^1\text{:}\eta^2\text{-}O_2)[Ca(OTf)]\}^{3+}$, **2**, can be synthesized via any sequence of addition of **[Cu^I]$^+$**, $Ca(OTf)_2$ and O_2 in acetone at low temperature (≤ 195 K) and are illustrated as Scheme S1. The specific general procedures are referenced when used for studies related to synthesis, spectroscopy, and reactivity. **Note**: A minimum of 5 equivalents of $Ca(OTf)_2$ relative to **[Cu^I]$^+$** is required to fully convert **1** to **2**.

Scheme S1. General procedures for synthesis of **2**

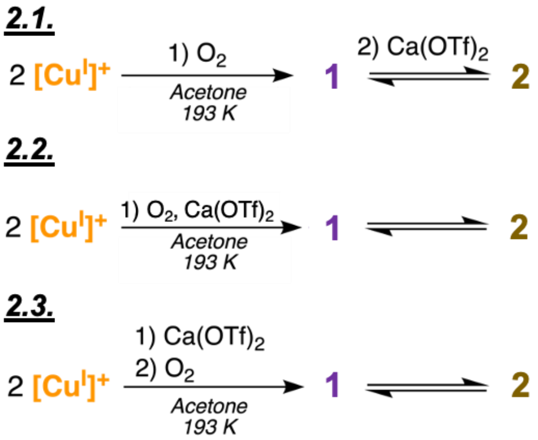

General Procedure 2.1. A 20 mM stock solution of **[Cu^I]$^+$** (27.0 mg, 0.05 mmol, MW: 539.93 g·mol^{-1}) in acetone was prepared in a N_2-filled glovebox. A small volume of stock solution (100 μL = 1 mM, 0.002 mmol) was added by a gas-tight syringe to an O_2-saturated acetone solution (1.7 mL) at 193 K. **1** was formed upon mixing, resulting in an immediate color change from light-orange to dark-purple. A small volume of concentrated $Ca(OTf)_2$ solution in acetone (100 mM, 0.02 mmol, MW: 338.22 g·mol^{-1}) was quickly injected (200 μL = 10 mM, 0.02 mmol, 10 equiv.) directly to **1** at 193 K, resulting in formation of dark-yellow **2**. **Note**: This procedure was carried out for [Cu^I]: 0.1 – 2 mM and [Ca]:[Cu] ranging 1:2 – 20:1.

General Procedure 2.2. A 20 mM stock solution of **[Cu^I]$^+$** (27.0 mg, 0.05 mmol, MW: 539.93 g·mol^{-1}) solution was prepared in a N_2-filled glovebox. A small volume of stock solution (100 μL = 1 mM, 0.002 mmol) was added by a gas-tight syringe to an O_2 saturated $Ca(OTf)_2$ acetone solution (1.9 mL, 10 mM, 0.02 mmol, 10 equiv., MW: 338.22 g·mol^{-1}) at 193 K and directly formed **2**. At low $Ca(OTf)_2$ concentrations (1-4 equivalents relative to **[Cu^I]$^+$**), some **1** was observed that eventually converts to **2** or decays at a proportional rate. **Note**: This procedure was carried out for [Cu^I]: 0.1 – 2 mM and [Ca]:[Cu] ranging 1:2 – 20:1.

General Procedure 2.3. **[Cu^I]$^+$** (27.0 mg, 0.05 mmol, 50 mM, MW: 539.93 g·mol^{-1}) and $Ca(OTf)_2$ (101.5 mg, 0.3 mmol, 300 mM, MW: 539.93 g·mol^{-1}) were dissolved in 1 mL of acetone in an N_2 glovebox and capped with septa to prevent air-exposure once removed. Vessel was then placed in a dry ice/acetone bath or liquid nitrogen and allowed to cool. A stainless-steel needle was then used to slowly bubble O_2 directly into solution or headspace. For solutions frozen in liquid nitrogen, sample was thawed at 193 K to allow reaction to occur, then refrozen. **Note**: This procedure was carried out for [Cu^I]: 1 – 50 mM and [Ca]:[Cu] ranging 5:1 – 10:1.

3. UV-Vis chemical reaction monitoring

UV-Visible absorbance spectra were collected on an Agilent Cary 8453 UV-vis spectrophotometer. A Unisoku USP-203 Cryostat cooled with liquid nitrogen was used for all low-temperature measurements. Unless specified otherwise, 1 cm pathlength quartz cuvettes were used for all measurements, and blanks were obtained in the measured solvent and reaction temperature. A custom Teflon holder (Figure S2) was used with standard 1 cm pathlength cuvettes to minimize any condensation during low temperature measurements.

Figure S2. Teflon holder used to grasp 1 cm cuvette and fit snuggly inside Cryostat chamber.

General ***procedures 2.1. and 2.2*** were used for chemical monitoring experiments. Small volumes (< 200 µL) of reagents were added to the cuvette solutions via an opening in Teflon holder that was capped with rubber septum between additions. Solutions containing $\mathbf{[Cu^{I}]^{+}}$ were prepared in the glovebox and handled using gas-tight syringes to prevent exposure to air and moisture.

The mixing time of reagents in our experiments were faster than the detector sampling time (500 ms). This was confirmed by addition of $CoCp_2$ using gas-tight syringes with rapid hand-injection into a cuvette sampling every 500 ms (Figure S3).

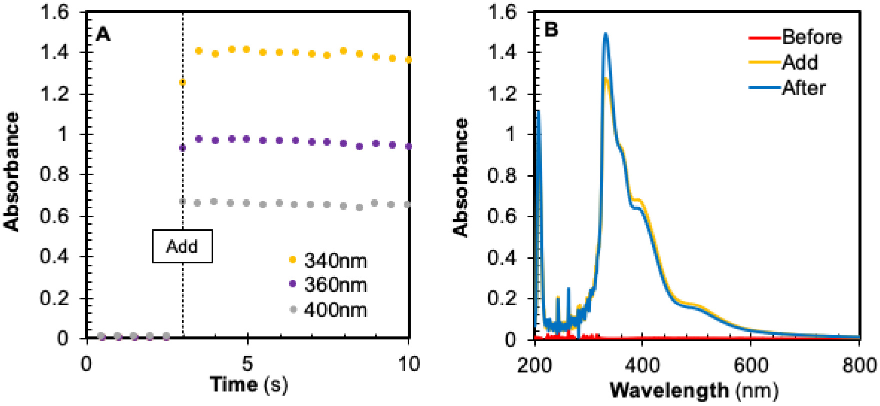

Figure S3. Demonstration of mixing time with the addition of $CoCp_2$ (200 µL; 20 mM acetone solution) via gas-tight syringe to a 1 cm cuvette charged with 1.8 mL acetone (1 mM $CoCp_2$ total; $\lambda_{max} = 332$ nm, $\epsilon = 750\ M\cdot cm^{-1}$) at 298 K. UV-vis spectra collected at 500 ms intervals. **(A)** time course **(B)** $CoCp_2$ absorption spectra during addition.

*3.1. Time course for interconversion between **1** and **2***

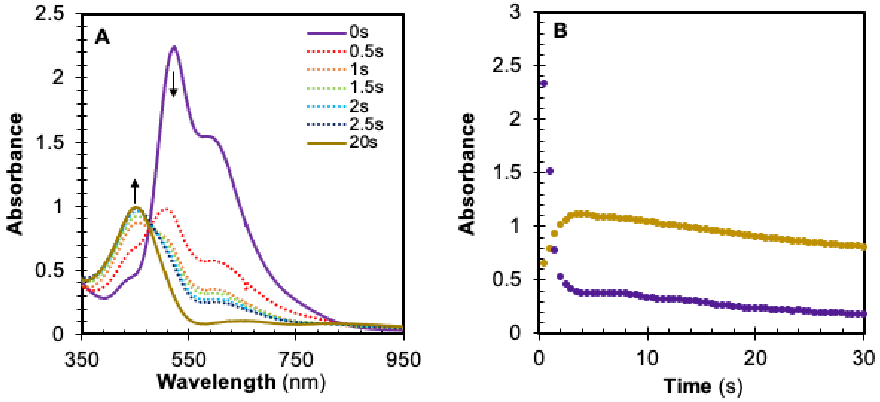

Figure S4. Addition of Ca(OTf)$_2$ (5 mM) to **1** (0.5 mM) in acetone (O$_2$ saturated) at 193 K. (A) Select UV-vis spectra over a 20 second range (B) Time course tracking absorbance at 455 nm (gold; **2**) and 600 nm (purple; **1**).

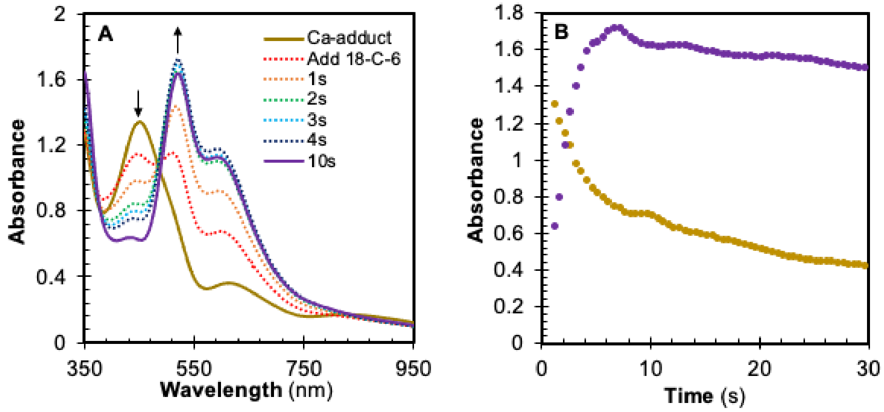

Figure S5. Addition of 18-crown-6 (10 mM) to **2** (0.5 mM) in acetone (O$_2$ saturated) at 193 K. (A) Select UV-Vis spectra over a 10 second range. (B) Time course tracking absorbance at 455 nm (gold; **2**) and 600 nm (purple; **1**).

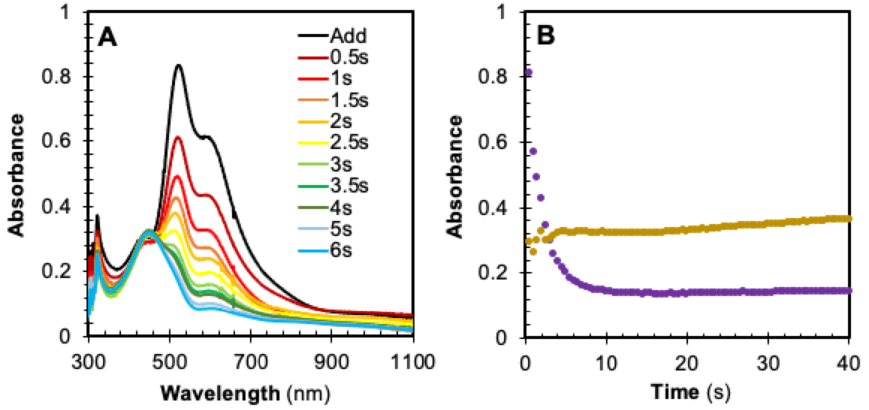

Figure S6. Addition of **[Cu^{I}]$^{+}$** (0.2 mM) to Ca(OTf)$_2$ (2 mM) in acetone (O_2 saturated) at 193 K (A) Selected UV-Vis spectra over a 6 s range (B) Time course tracking absorbances at 455 nm (gold; **2**) and 600 nm (purple; **1**).

*3.3. Half-life **1** and **2***

At moderate concentrations (~0.25 mM), both **1** and **2** slowly decompose at 193 K in acetone (Figure S7). The $t_{1/2}$ of **1** and **2** were determined by monitoring the absorbance decrease with respect to time at 525 nm (ε = 8580 L mol^{-1} cm^{-1}; $t_{1/2}$ = 150 s) and 455 nm (ε = 4080 L mol^{-1} cm^{-1}; $t_{1/2}$ = 285 s), respectively (Figure S8). **1** has been reported to oxidize PF_6^{-} counter ion forming fluoride bound Cu^{II} products,[7] and further investigation of the decomposition products are currently underway.

It was noted that addition of triflate anion in the form of [NBu$_4$][OTf] significantly improves the stability of **1** (0.1 mM) in acetone at 193 K (Figure S9; **1**, $t_{1/2}$ = 60 s; + 2 mM [NBu$_4$][OTf], $t_{1/2}$ = 170 s). The presence of triflate counter ion does not lead to any new features/changes in the UV-Visible spectra until high concentrations (> 20 equiv relative to CuTMPA), where triflate binding to **[Cu^{II}]$^{2+}$** leads to a weak feature at 470 nm (Figure S10; ϵ = 250 M^{-1}·cm^{-1}).

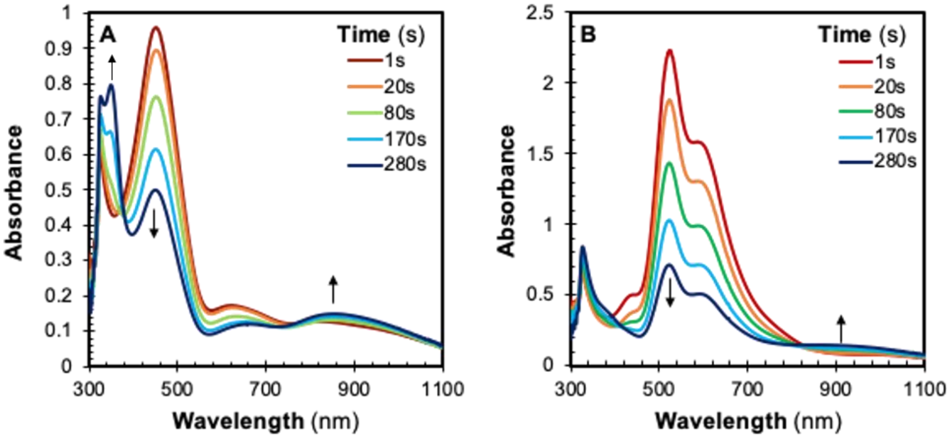

Figure S7. Decomposition in acetone (O_2 saturated; 193 K) of (A) **2** (0.25 mM, Ca(OTf)$_2$ = 5 mM; λ_{max} = 455 nm) and (B) **1** (0.25 mM, λ_{max} = 525 nm). **Note**: **[Cu^{II}]$^{2+}$** (λ_{max} = 880 nm).

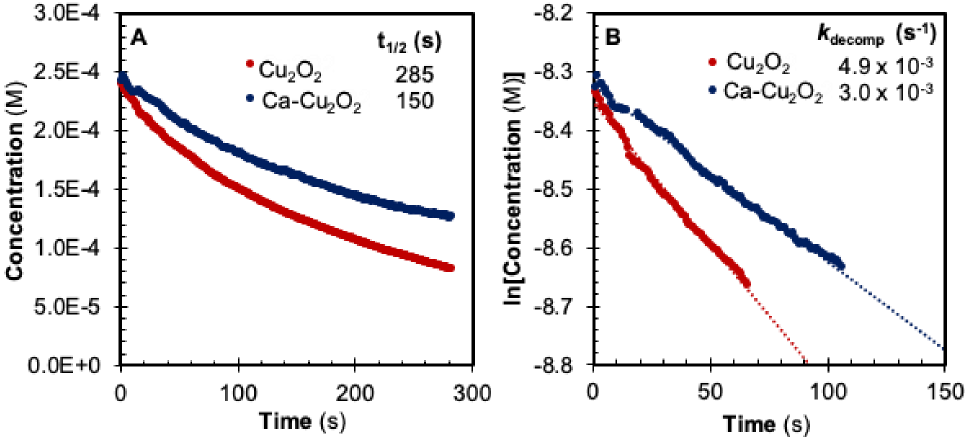

Figure S8. $t_{1/2}$ determination of **2** and **1** under the conditions described in Figure S7 plotted as (A) concentration *vs* time and (B) natural log of concentration *vs* time.

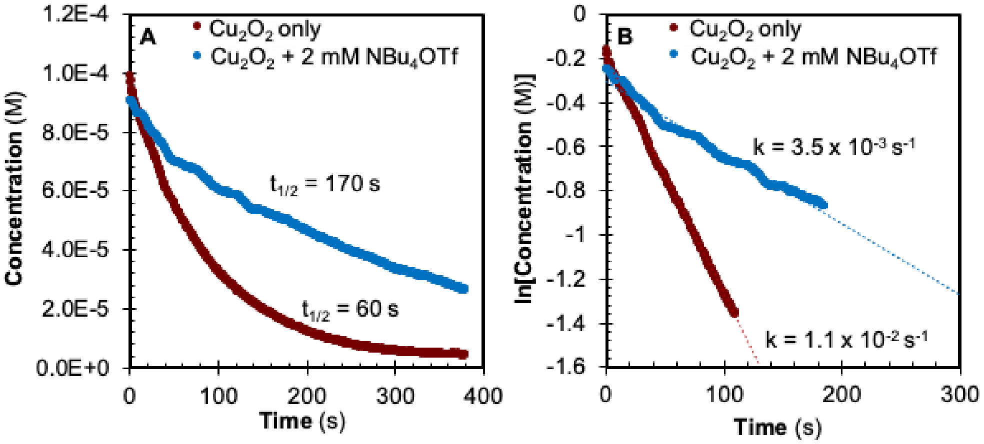

Figure S9. Decomposition in acetone (O_2-saturated; 193 K) of **1** (0.1 mM, λ_{max} = 525 nm) in the absence (red trace) and presence (blue trace) of [NBu$_4$][OTf] (2 mM). (A) decay *vs* time (B) natural log of concentration *vs* time.

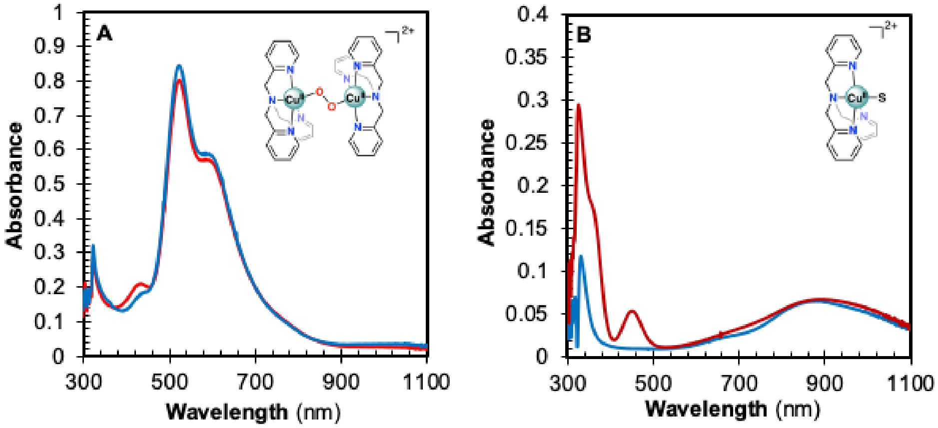

Figure S10. UV-Vis spectra in acetone (O_2-saturated; 193 K) of (A) **1** (0.1 mM; blue trace) and **1** (0.1 mM) with [NBu$_4$][OTf] (2 mM; red trace) and (B) **[Cu^{II}]$^{2+}$** (0.2 mM; blue trace) and **[Cu^{II}]$^{2+}$** (0.2 mM) with [NBu$_4$][OTf] (30 mM; red trace).

3.4. Association constant (K_a) determination

A binding constant was determined by adding varying amounts of $Ca(OTf)_2$ to **1** according to general ***procedure 2.2.*** while monitoring UV-Vis features every 500 ms. Data was collected from individual measurements instead of a continuous titration due to the instability of both compounds at low concentrations. Spectra and absorbances were selected from early time points where both conversion was complete and there was not yet significant decomposition of either species in equilibrium (Figure S11). The 525 nm λ_{max} of **1** overlaps with the 455 nm λ_{max} of **2** leading to inflated absorptivity for both species if not corrected (Figure S11b). The secondary absorption feature of **1** at 600 nm (ε = 5940 L mol^{-1} cm^{-1}) does not significantly overlap with **2** features and was used to correct 525 nm and 455 nm absorbances (Figure S11c).

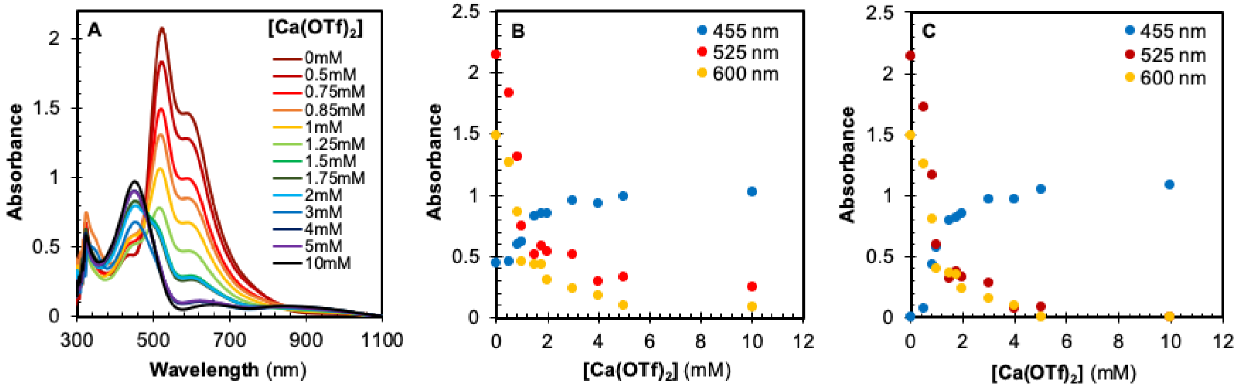

Figure S11. (A) UV-Vis spectra of $Ca(OTf)_2$ (0–10 mM) concentrations added to **1** (0.5mM, λ_{max} = 525, nm ε = 8580 L mol^{-1} cm^{-1}; λ = 600 nm, ε = 5940 L mol^{-1} cm^{-1}) converting to **2** (0–0.5mM, λ_{max} = 445 nm, ε = 4080 L mol^{-1} cm^{-1}), (B) uncorrected absorbances, (C) absorbances corrected using 600 nm absorbance of **1**.

Uncorrected and corrected absorbances from Figure S11 were used to calculate the association constant using the MatLab® program reported by Thordarson.[8] Data was fit as a 1:1 complexation event where **1** was the host and Ca^{II} was the guest (Equations S1 and S2). Higher-order binding equilibria (e.g. 1:2, [Cu]:[Ca]) were also attempted, but resulted in very poor fits (e.g. asymptotic error > 500%). Corrected and uncorrected absorbances resulted in similar values of calculated K_a, 1220 M^{-1} (± 35% asymptotic error). The asymptotic error was deemed acceptable due to the inherent instability of both complexes and the necessity to measure $Ca(OTf)_2$ additions individually instead of a continuous titration. Further Monte Carlo simulations were used to determine confidence intervals, where the lower confidence was 1149 M^{-1} and higher confidence was 1284 M^{-1}.

For a 1:1 complex:

$$\mathrm{H} + \mathrm{G} \overset{K_a}{\rightleftarrows} \mathrm{HG}$$

Eq. S1

$$[\mathrm{HG}] = \frac{1}{2}\left(\left([\mathrm{G}]_0 + [\mathrm{H}]_0 + \frac{1}{K_a}\right)^2 + 4\,[\mathrm{H}]_0[\mathrm{G}]_0\right)^{1/2}$$

Eq. S2

$[H]_0$ = Initial host concentration
$[G]_0$ = Initial guest concentration

*3.5. Determining kinetic parameters for conversion of **1** to **2***

Kinetics values for **1** to **2** conversion were obtained from monitoring reactions using UV-Vis using ***procedure 2.1.*** Given Ca^{II} binding to **1** was found to be a reversible reaction, the rate at which **1** converts to **2** under flooding conditions (> 10-fold excess $Ca(OTf)_2$ relative to **1**) reduces to that of a simple reversible first-order reaction. Determination of k_{obs} by varying $Ca(OTf)_2$ concentrations allows for the determination of the forwards (k_{+1}) and backwards (k_{-1}) rate constants using equations S3-S10 and the association constant obtained in **Section 3.4** (K_a=1220 M^{-1}).[9] Values of k_{obs} (s^{-1}) for the conversion of **1** to **2** were obtained by using excess [$Ca(OTf)_2$] and monitoring the decrease in absorbance profile at 600 nm (ε = 5940 L mol^{-1} cm^{-1}). First-order decay plots are displayed in Figure S12a, and saturation was achieved at 10 mM $Ca(OTf)_2$ (Fig S12c).

At equilibrium:

$$[\mathbf{2}]_0 + [\mathbf{1}]_0 = [\mathbf{2}]_{eq} + [\mathbf{1}]_{eq} \qquad \textbf{Eq. S3}$$

$$[\mathbf{2}]_{eq} + [\mathbf{1}]_{eq} = 0.5\text{ mM} \qquad \textbf{Eq. S4}$$

With 1 mM $\mathbf{[Cu^I]^+}$, concentration of bound + unbound dimer will be equal to 0.5 mM, hence Eq. S3 rearranges to Eq. S4 and can be employed to simplify Eq. S6

$$k_{+1}[\mathbf{1}]_{eq} = k_{-1}[\mathbf{2}]_{eq} \qquad \textbf{Eq. S5}$$

$$K_a = \frac{[\mathbf{2}]}{[\mathbf{1}][Ca(OTf)_2]} = \frac{0.5\text{mM} - [\mathbf{1}]}{[\mathbf{1}][Ca(OTf)_2]} \qquad \textbf{Eq. S6}$$

Plotting $ln\{[\mathbf{1}]_t - [\mathbf{1}]_{eq}\}$ measured during time course subtracted from $[\mathbf{1}]_{eq}$ calculated from Eq. S6 *vs* time leads to linear relationship where slope (k_e) can be used to calculate k_{+1} and k_{-1}

$$\ln([\mathbf{1}]_t - [\mathbf{1}]_{eq})\ \textit{vs}\ \text{time where slope} = k_e \qquad \textbf{Eq. S7}$$

$$k_e = k_{+1}[Ca(OTf)_2]_0 + k_{-1} \qquad \textbf{Eq. S8}$$

$$k_{-1} = \frac{k_e}{1 + K[Ca(OTf)_2]_0} \qquad \textbf{Eq. S9}$$

$$k_1 = \frac{k_e}{K[Ca(OTf)_2]_0 + K^{-1}} \qquad \textbf{Eq. S10}$$

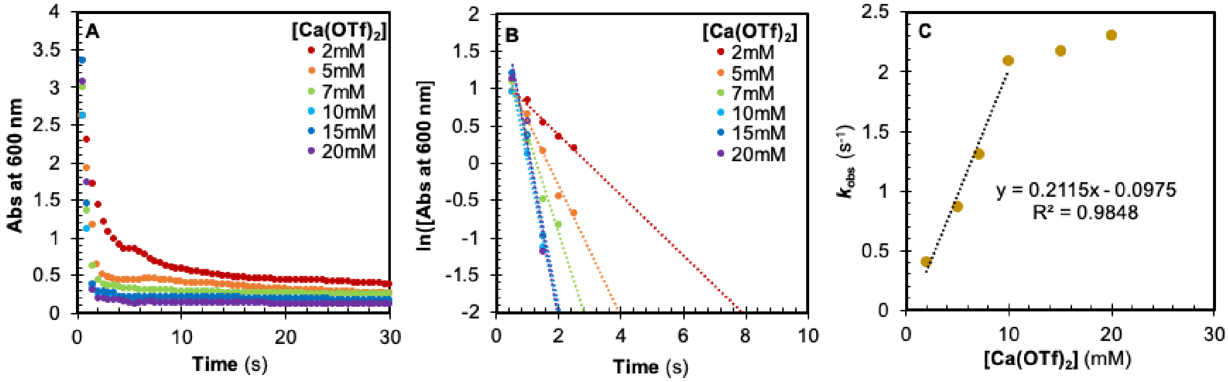

Figure S12. (A) Decay of **1** (0.5 mM, 600 nm) after $Ca(OTf)_2$ (2-20 mM) addition, (B) natural log of concentration of **1** (0.5 mM, 600 nm) *vs* time, (C) k_{obs} *vs* $[Ca(OTf)]_2$, where saturation was observed ≥ 10 mM $[Ca(OTf)_2]$.

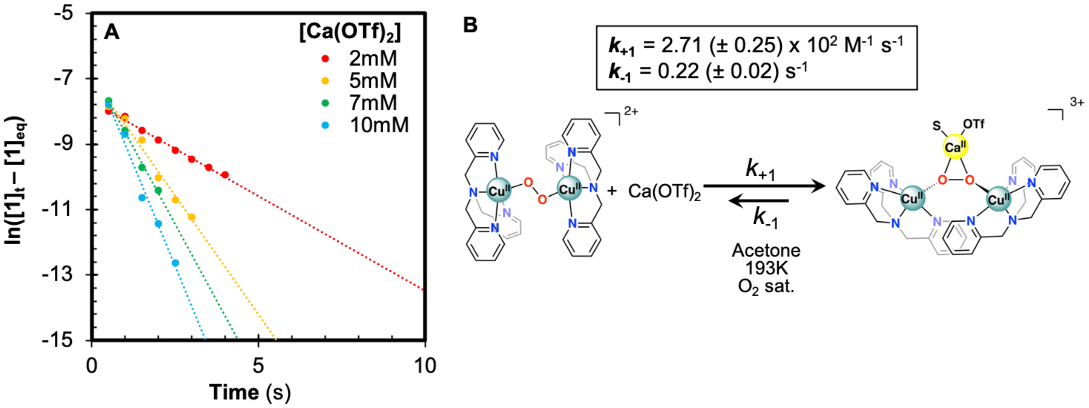

Figure S13. (A) $\ln([\mathbf{1}]_t - [\mathbf{1}]_{eq})$ given amount of $Ca(OTf)_2$ (2-10 mM) plotted *vs* time where slope is used to calculate forwards (k_{+1}) and backwards (k_{-1}) rate constants, (B) Scheme for equilibria between **1** (left) and **2** (right) where k_{+1}= 2.71 (± 0.25) × 10^2 M^{-1} s^{-1} and (k_{-1})= 0.22 (± 0.02) s^{-1}.

Scheme S2. Chemical steps believed to lead to formation of **2**

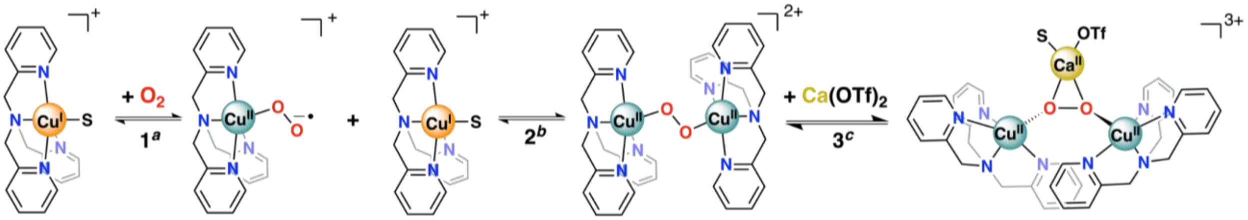

Table S1. Kinetic and equilibrium parameters of chemical steps outlined in Scheme S2 (above) leading to **2**

Reaction	**1^a**	**2^b**	**3^c**
K (M^{-1})	6.5 × 10^5	5 × 10^{10}	1.2 (± 0.07) × 10^3
k_+ (M^{-1} s^{-1})	1.6 × 10^8	1.0 (± 0.2) × 10^5	2.2 (± 0.4) × 10^2
k_- (M^{-1} s^{-1})	240	2 × 10^{-6}	1.8 (± 0.3) × 10^{-1}

a O_2 binding to **$[Cu^I]^+$** to form monomeric superoxide in THF at 193 K[10], ***b*** Dimerization of $\{CuO_2\}^{\bullet-}$ and **$[Cu^I]^+$** to form **1** in THF at 183 K[5c], ***c*** $Ca(OTf)_2$ binding to **1** in acetone at 193 K (this work).

*3.6. Formation of **2** with Ca(ClO$_4$)$_2$*

Calcium perchlorate (Anhydrous 99%, Sigma) was used to compare reactivity a non-coordinating counter ion other than triflate via ***procedure 2.2.*** While **2** does form with Ca(ClO$_4$)$_2$, the conversion from **1** to **2** is not complete even with high concentrations of Ca(ClO$_4$)$_2$ (17 equivalents relative to **[Cu^I]**$^+$). Although the Ca(ClO$_4$)$_2$ was handled in the glovebox, we hypothesize the material had a significant amount of moisture despite being purchased as anhydrous; hence, the **2** formed decomposed relatively quickly compared to when Ca(OTf)$_2$ is used as a calcium source (Figure S14). When [NBu$_4$][OTf] is added along with Ca(ClO$_4$)$_2$, conversion from **1** to **2** improves, but **2** still decomposes quickly (Figure S15). When H$_2$O is added to **2** (0.5 mM) formed with Ca(OTf)$_2$ (5 mM), the adduct decomposes at about the same rate as when Ca(ClO$_4$)$_2$ is used as a calcium source (Figure S16). This further validates Ca^{II} binding is involved in formation of the species observed at 455 nm, and that [OTf]$^-$ counter ion may play a role in conversion and stability. We hypothesize **2** decays by reacting with excess moisture to form {[Cu(TMPA)]$_2$(μ-OH)}$^{3+}$. Support for this comes from the growth of a characteristic high-energy absorption feature at 351 nm (Figure S14) and ^{1}H NMR spectral features (Figure S29) that are similar to that reported by Kieber-Emmons.[11] The reactivity of **2** will be reported in due course.

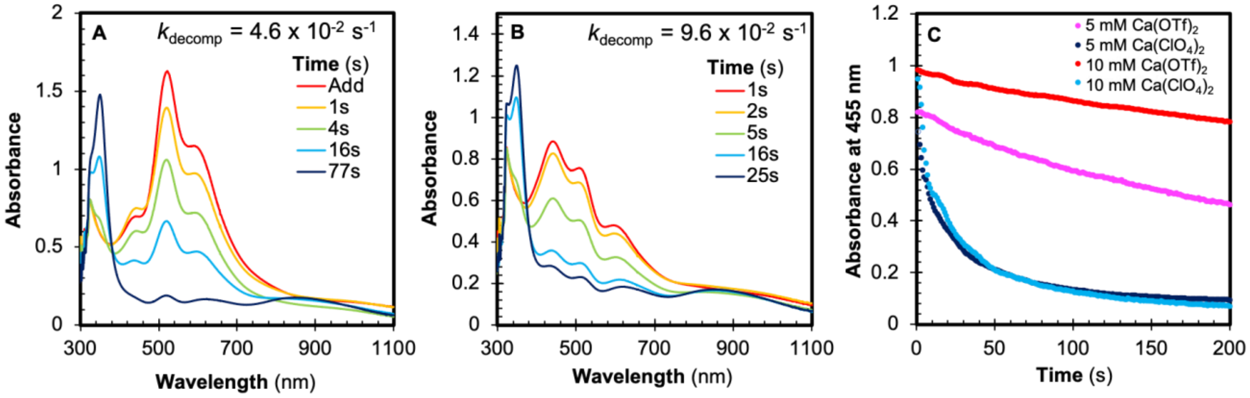

Figure S14. UV-Vis spectra in acetone (O$_2$-saturated, 193 K) after **[Cu^I]**$^+$ (1 mM) addition to Ca(ClO$_4$)$_2$ solutions, (A) [Ca] = 5 mM, (B) [Ca] = 17 mM, (C) Time course following the decay of **2** (0.5 mM; λ_{max} = 455 nm) formed with either Ca(OTf)$_2$ (pink: 5 mM; red: 10 mM) or Ca(ClO$_4$)$_2$ (navy: 5 mM; light-blue: 10 mM).

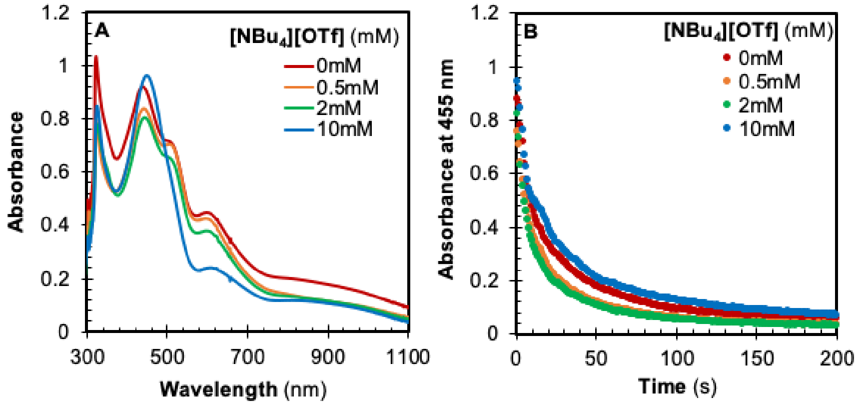

Figure S15. Addition in acetone (O$_2$-saturated, 193 K) of **[Cu^I]**$^+$ (1 mM) and varying amounts of [NBu$_4$][OTf] (0 – 10 mM) to 10 mM Ca(ClO$_4$)$_2$ solutions, (A) UV-Vis spectra upon addition, (B) Time course following the decay of **2** (0.5mM, λ_{max} = 445 nm).

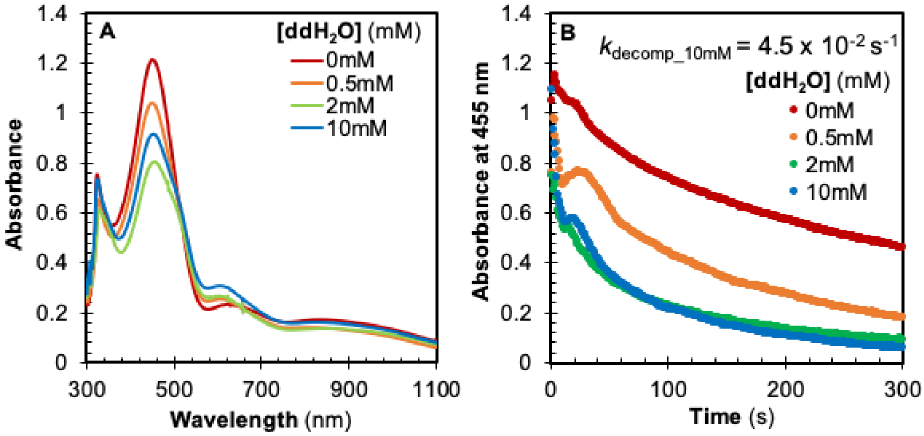

Figure S16. Addition in acetone (O_2-saturated, 193 K) of H_2O (0-10 mM) to **2** (0.5 mM, $Ca(OTf)_2$ = 5 mM), (A) UV-Vis spectra upon addition, (B) Time course following the decay of **2** (0.5 mM, λ_{max} = 445 nm).

*3.7. UV-Vis of $Ca(OTf)_2$ binding to species other than **1***

While rRaman and EPR studies strongly disfavor monomeric Cu^{II} species as plausible structures of **2**, we included several additional controls to safely establish that the UV-Visible spectroscopic features were not due to ligand dissociation or a monomeric Cu^{II} peroxido bound to calcium.

Upon addition of $Ca(OTf)_2$ to tris(2-pyridylmethyl)-amine (TMPA), a weak UV-vis feature was observed at 415 nm at room temperature in acetone, but its molar absorptivity coefficient is much smaller than that of **2** (Ca(TMPA): ε = 100 M^{-1} cm^{-1}; **2**: ε = 4,080 M^{-1} cm^{-1}; Figure S17). Ca^{II} binding to TMPA was also confirmed by ^{1}H NMR, where clear shifts in the pyridyl protons were observed in the presence of excess $Ca(OTf)_2$ (Figure S24). Addition of excess $Ca(OTf)_2$ to **$[Cu^I]^+$** did not lead to significant shifts in the pyridyl proton resonances, and therefore was considered to not have a significant binding interaction under N_2 atmosphere (*vide infra*, Figures S25).

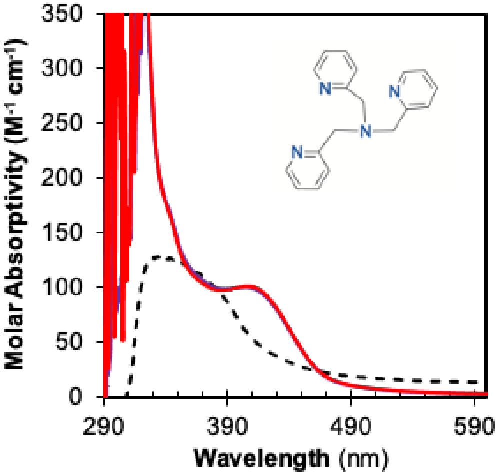

Figure S17. UV-Vis spectra of tris(2-pyridylmethyl)-amine in acetone (20 mM) at room temperature (black dotted trace); addition of 1 equivalent $Ca(OTf)_2$ (blue trace) and 2 equivalents $Ca(OTf)_2$ (red trace) lead to new feature at 415 nm (ε = 100 M^{-1} cm^{-1}).

The monomeric copper η^1-hydroperoxido, [Cu^{II}(TMPA)(OOH)]$^+$, can be generated at low temperature with urea hydrogen peroxide (UHP) and triethylamine (NEt_3).[12] To exclude the possibility of forming a dinuclear heterobimetallic species such as {[Cu^{II}(TMPA)](μ-1,2-O_2^{2-})[Ca($OTf)_2$(sol)$_n$]}, the reaction of Ca($OTf)_2$ with [Cu^{II}(TMPA)(OOH)]$^+$ was explored (Figure S18). [Cu^{II}(TMPA)(OOH)]$^+$ was generated in acetone solutions (N_2-saturated) at 193 K by adding NEt_3 (0.5 mM, 1.67 equiv) to a mixture of **[Cu^{II}]$^{2+}$** (0.3 mM, 1 equiv) and UHP (1.5 mM, 5 equiv). Addition of Ca($OTf)_2$ (3 mM, 10 equiv) to [Cu^{II}(TMPA)(OOH)]$^+$ leads to bleaching (< 500 ms) of the feature at 410 nm with no observable intermediate(s).

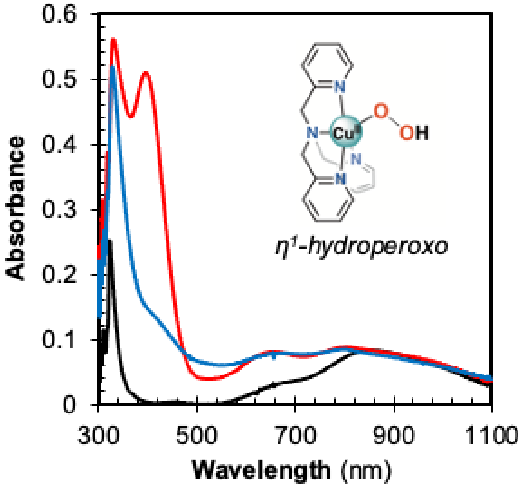

Figure S18. UV-Vis spectra of **[Cu^{II}]$^{2+}$** (0.3 mM) and UHP (1.5 mM) in acetone (N_2-saturated, 193K) (black trace); addition of NEt_3 (0.5 mM) to form [Cu^{II}(TMPA)(OOH)]$^+$ (0.3 mM; red trace); addition of Ca($OTf)_2$ (3 mM; blue trace)

4. EPR measurements

EPR spectra were collected on a Bruker EMX Premium-X spectrometer with a field strength of 9.65 GHz and a microwave power of 2.0 mW at 77 K using a liquid-nitrogen finger dewar (Wilmad, 50 mL Suprasil) using 4 mm O.D. quartz tubes (Wilmad). Sample solutions were prepared in acetone and 1:1 acetone:toluene (improved glass formation).[13] Glasses were prepared by slowly lowering the sample into liquid nitrogen (~2 mm / s). Spectra of $[Cu^{II}(TMPA)(CH_3CN)(ClO_4)_2]$ matched literature reports (Figure S19).[14]

2 and **1** were generated according to ***procedure 2.3.*** with toluene included in EPR tubes capped with septa. **2** was determined to be EPR silent at X-band frequencies, where no significant signal was observed above background. Some signal was present in **1** most likely due to some degradation but was not significant compared to background noise and signal did not improve with more scans (Figure S20). Noise due to moisture accumulation on inside of liquid-nitrogen finger dewar during measurements.

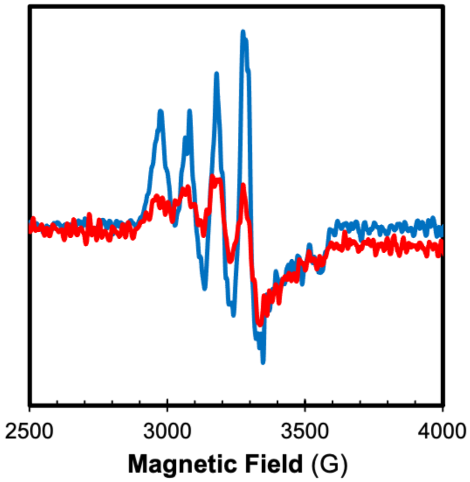

Figure S19. EPR spectra (9.65 GHz, 77 K) of $[Cu^{II}(TMPA)(CH_3CN)(ClO_4)_2]$ (1 mM) in acetone (10 scans, red trace) and 1:1 acetone:toluene (10 scans, blue trace).

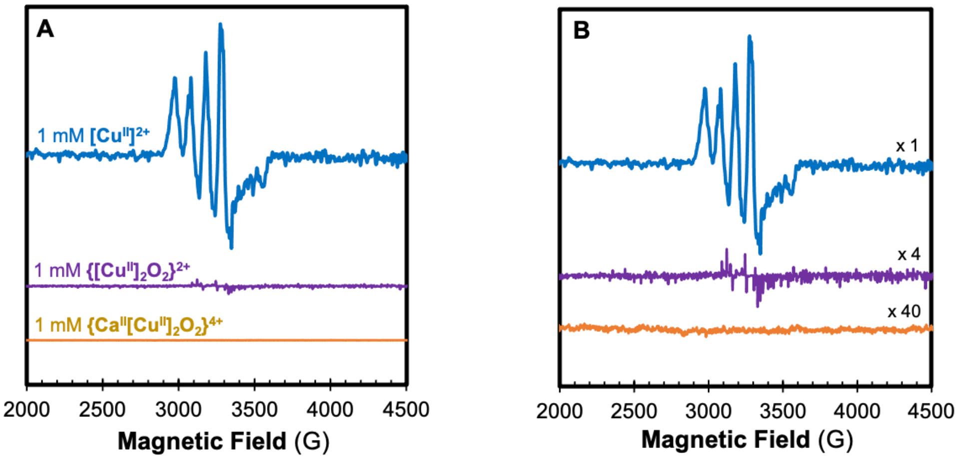

Figure S20. EPR spectra (9.65 GHz, 77 K, 1:1 acetone:toluene) of $[Cu^{II}(TMPA)(CH_3CN)(ClO_4)_2]$ (1 mM, blue trace), **1** (1 mM, purple trace), **2** (1 mM, gold trace); (A) traces normalized to number of scans, (B) traces multiplied to show baseline.

5. Resonance Raman measurements

Resonance Raman samples were prepared in a glovebox using the following procedure. 4 mm O.D. quartz EPR tubes (Wilmad) were charged with 500 µL of **$[Cu^I]^+$** (3–5 mM) in dry acetone (N_2-saturated). For samples of **2**, $Ca(OTf)_2$ was also added (15–25 mM). The EPR tubes were capped tightly with a septum and removed from the glovebox. The samples oxygenated according to ***procedure 2.3.*** in liquid nitrogen where O_2 gas ($^{16}O_2$ or $^{18}O_2$) was added to the headspace with a gas-tight syringe (10 mL). The tubes were then flame-sealed, thawed at –115 °C (dry-ice/pentane bath), and vigorously shaken to generate the peroxide species, **1** and **2**. The samples were then frozen again with liquid nitrogen and stored in a dry-shipper (pre-conditioned with liquid nitrogen) until measured.

The resonance Raman experiments were performed using a Cobolt 08-DPL laser at an excitation wavelength of 456.8 nm with 20mW power. Samples were transferred to a liquid nitrogen bath inside an EPR coldfinger to cool the samples during the measurements. The scattered light from the samples was focused onto an Acton two-stage TriVista 555 monochromator and detected by a liquid N_2-cooled Princeton Instruments Spec-10:400B/LN CCD camera. The accumulation and exposure times for the samples are specified in the figure captions below. The spectral resolution was 0.3 cm^{-1}. Spectra were then plotted and processed using the OriginPro 9.0.0 (64-bit) software for baseline correction.

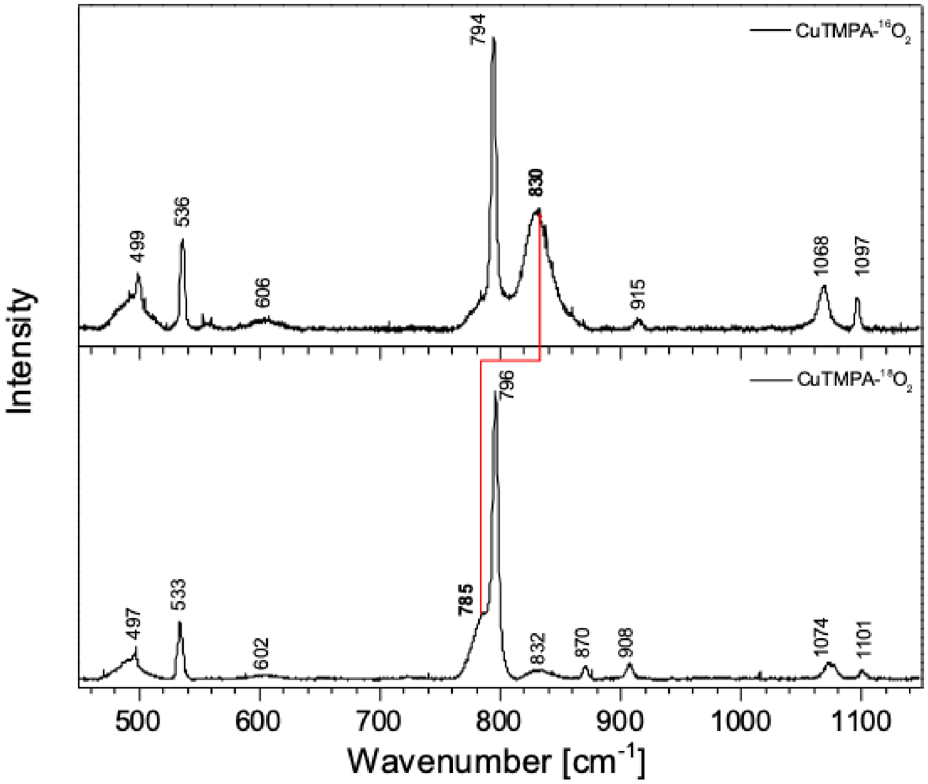

Figure S21. Resonance Raman spectra (457 nm excitation, 77 K) of **1** (2.5 mM) formed with $^{16}O_2$ (top) and $^{18}O_2$ (bottom). Spectra were collected in one accumulation with an exposure time of 5 min.

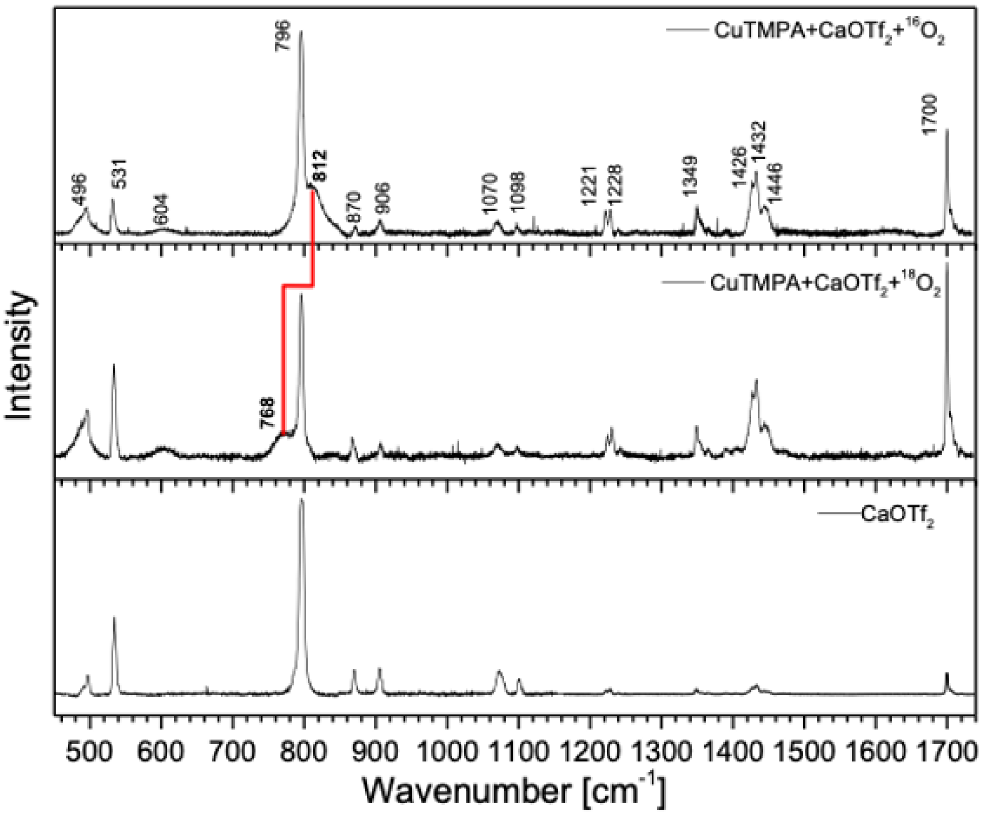

Figure S22. Resonance Raman spectra (457 nm excitation, 77 K) of **2** (1.5 mM) formed with $^{16}O_2$ (top) and $^{18}O_2$ (middle), and $Ca(OTf)_2$ (15 mM) in acetone (bottom). Spectra were collected in one accumulation with an exposure time of 60 s.

6. NMR measurements

All NMR spectra were collected on a Bruker Avance III HD Ascend (^{1}H: 600 MHz, ^{13}C: 152 MHz, ^{19}F: 564.5 MHz). ^{1}H NMR shifts are referenced relative to internal standard due to potential acetone binding to compounds (($SiMe_3$)$_2$O ^{1}H = 0.07 ppm; d_6-acetone ^{1}H ~ 2.05 ppm). A 600 MHz z-BBO probe was used to lock onto the ^{19}F nucleus on the ^{1}H channel and was referenced to an external standard ($[PF_6]^-$: ^{19}F = –72 ppm). All samples were prepared in an N_2-filled glovebox in either J. Young tubes (New Era) or standard 5 mm O.D. tubes. **1** and **2** were prepared according to ***procedure 2.3*** and then sparged with N_2 to remove excess O_2 in solution. The coaxial insert (Wilmad) was then slowly inserted into the sample tube and capped with a septum.

6.1. NMR spectra of non-Cu containing compounds

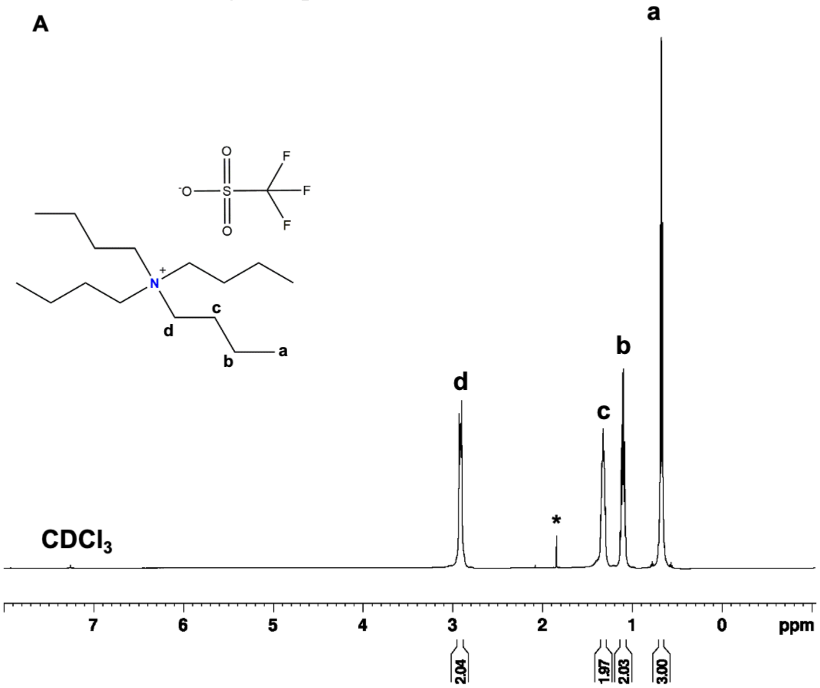

Figure S23a. ^{1}H NMR spectra ($CDCl_3$, 298 K) of $[NBu_4][OTf]$ (500 mM) (* represents residual water).

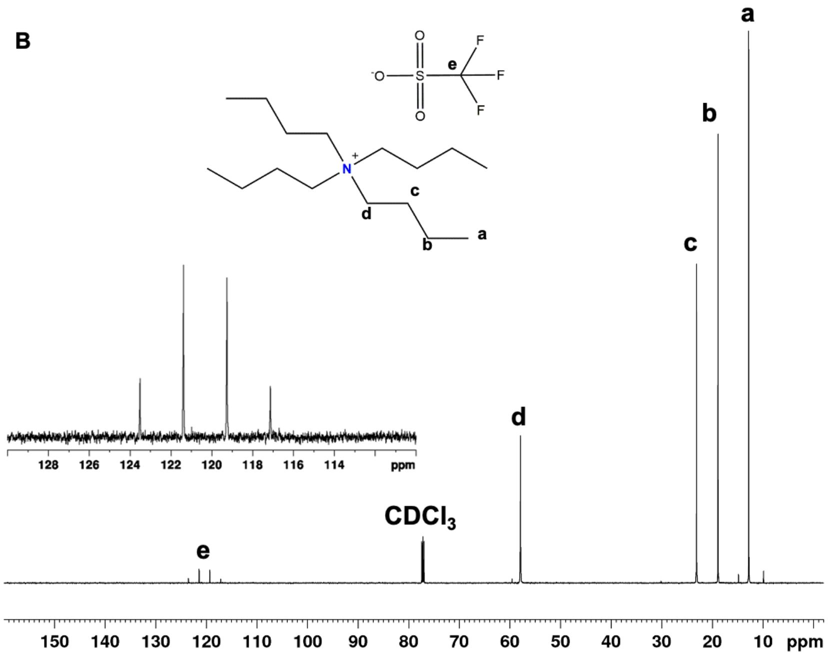

Figure S23b. $^{13}C\{^1H\}$ NMR spectra ($CDCl_3$, 298 K) of $[NBu_4][OTf]$ (500 mM).

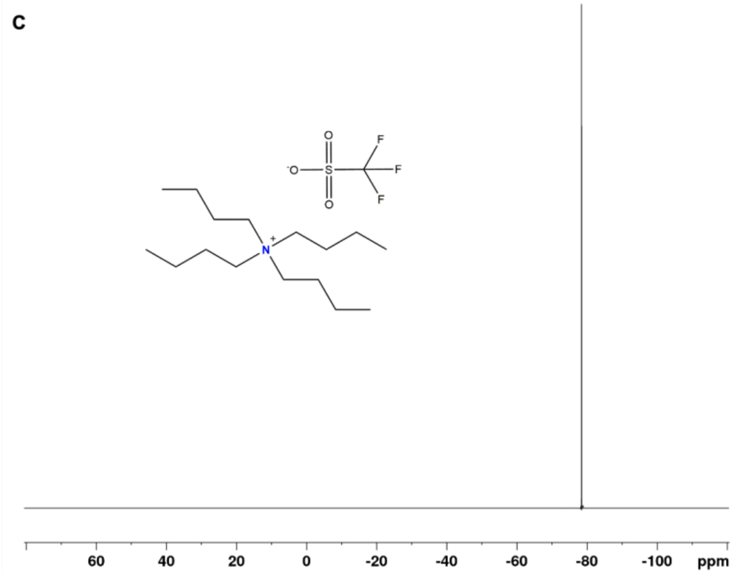

Figure S23c. $^{19}F\{^1H\}$ NMR spectra ($CDCl_3$, 298 K) of $[NBu_4][OTf]$ (500 mM).

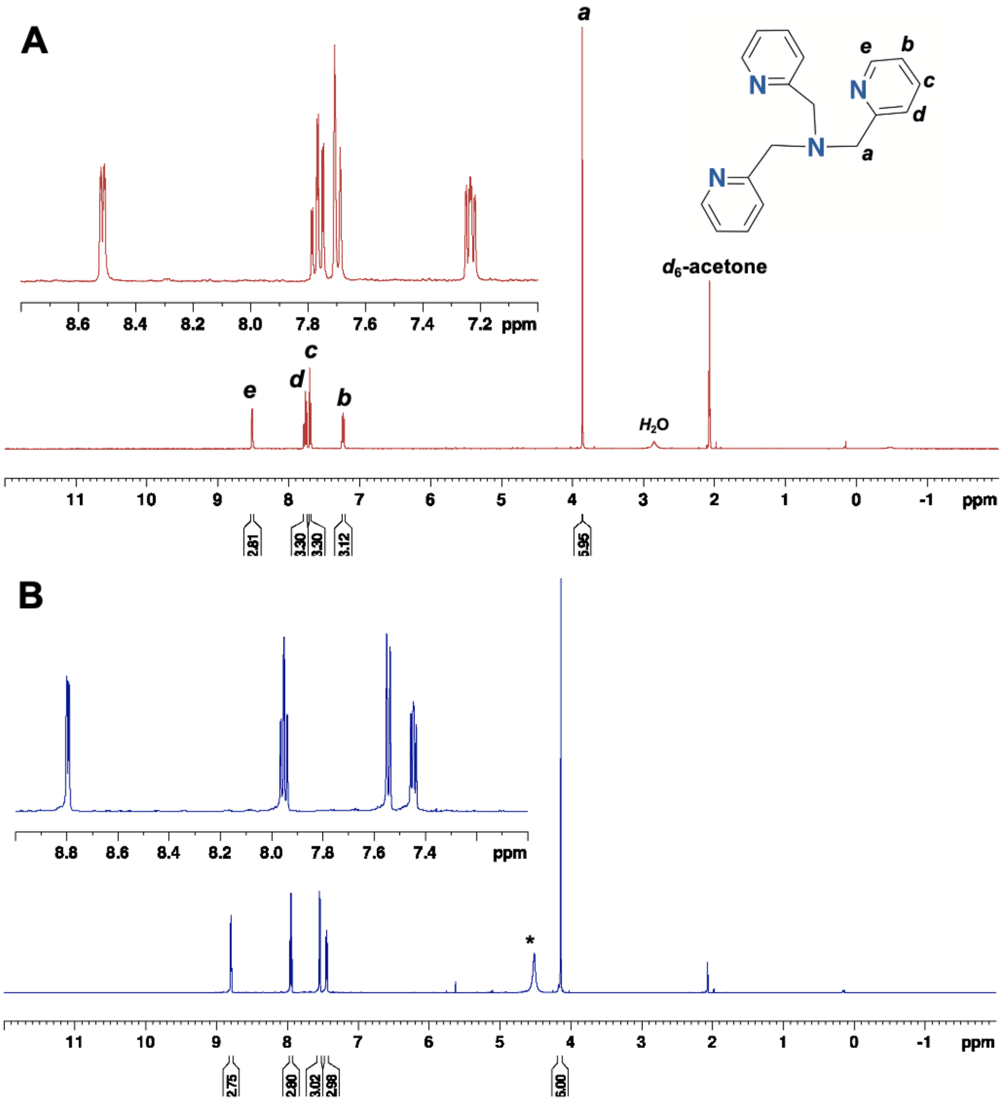

Figure S24. ^{1}H NMR spectra (d_6-acetone, 298 K) of **(A)** TMPA (5 mM), **(B)** TMPA (10 mM) + Ca(OTf)$_2$ (50 mM) (* represents Ca^{II} bound acetone or residual H_2O). Insets of 7-9 ppm represent pyridyl protons; no peaks were observed below 4 ppm or above 9 ppm).

6.2. ^{1}H NMR of Cu compounds

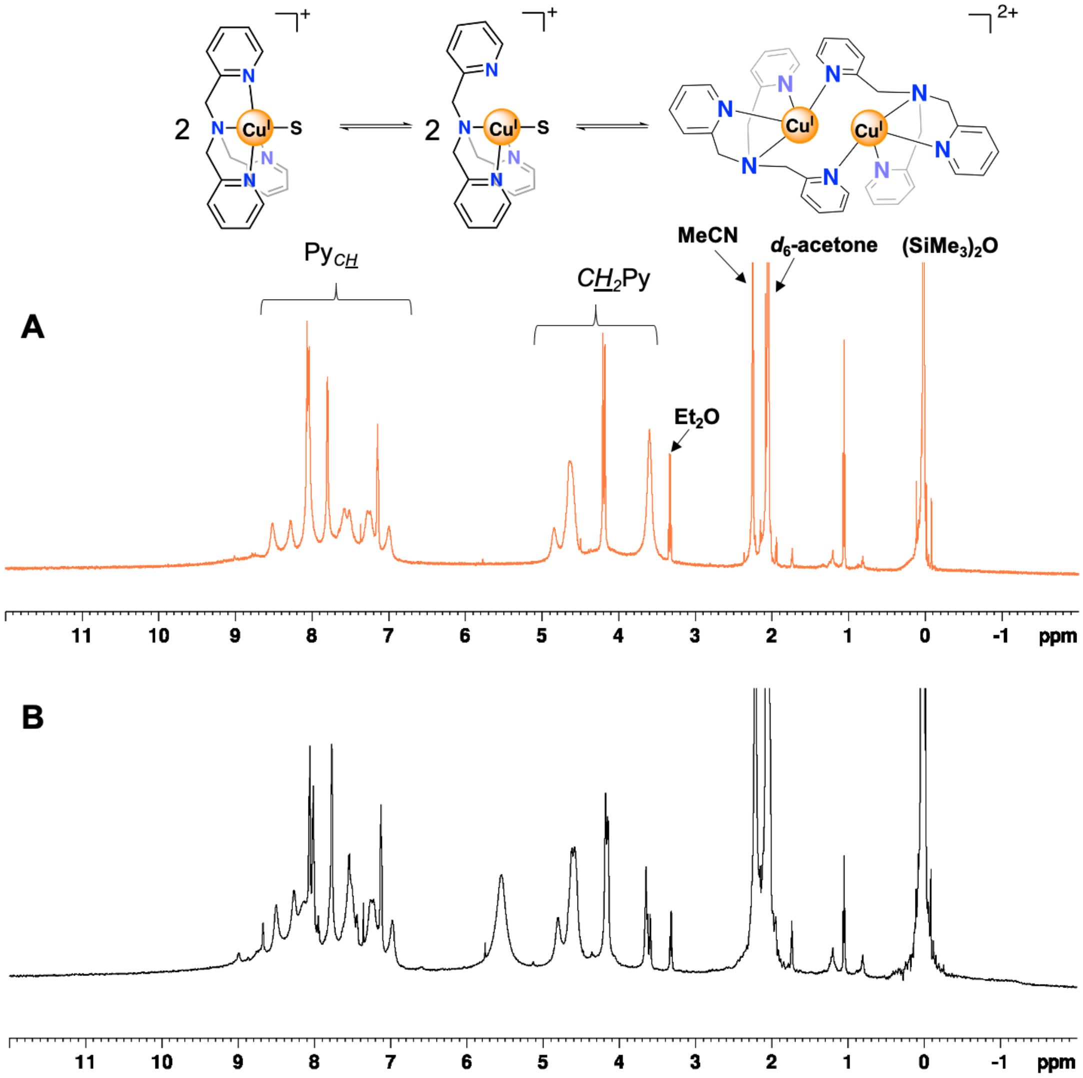

Figure S25. ^{1}H NMR spectra (d_6-acetone, 193 K) of **(A) [Cu^I]$^+$** (4 mM), **(B) [Cu^I]$^+$** (4 mM) + Ca(OTf)$_2$ (40 mM). **[Cu^I]$^+$** matches that reported by Karlin, et. al.,[5c, 15] where the broadness and lowered solution symmetry has been attributed to the formation of a dimer that is stabilized from additional π-stacking of the pyridyl arms in TMPA. **Note:** Peaks calibrated to the internal standard, $(SiMe_3)_2O$ (5 mM).

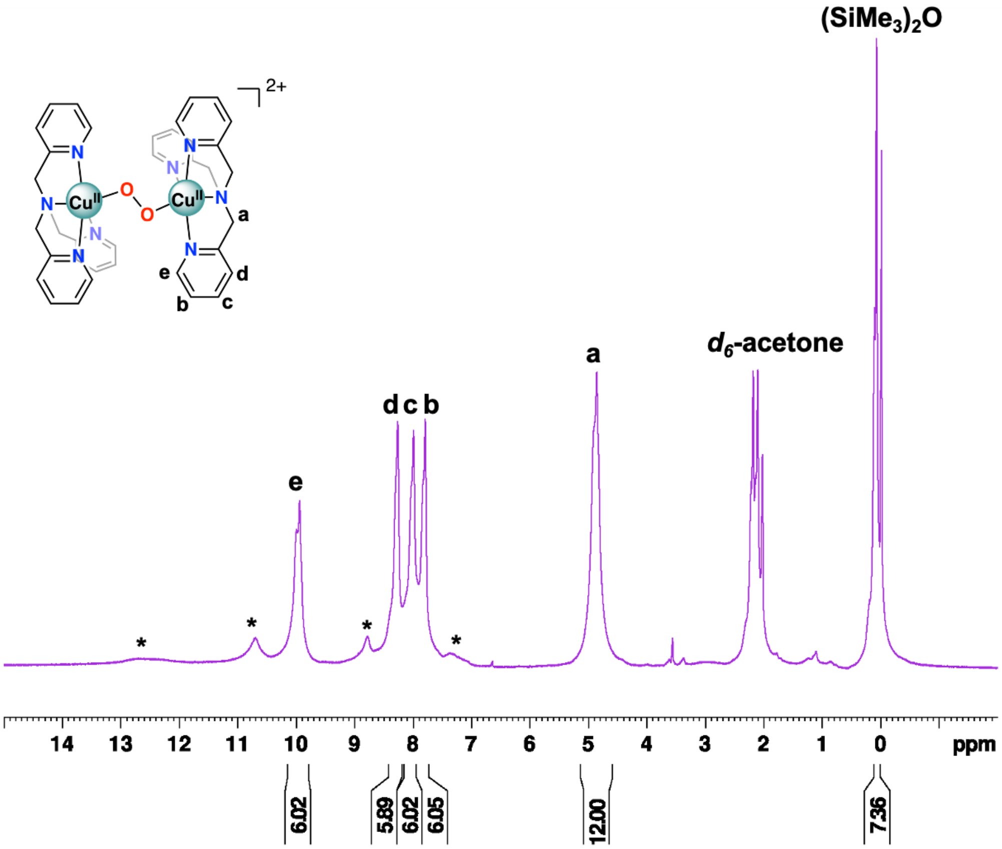

Figure S26. ^{1}H NMR spectra (d_6-acetone, 193 K) **1** (25 mM) (* = minor degradation product (paramagnetic)). **1** matches that reported by Karlin, et. al,[3] taken in CD_2Cl_2 at 185 K.

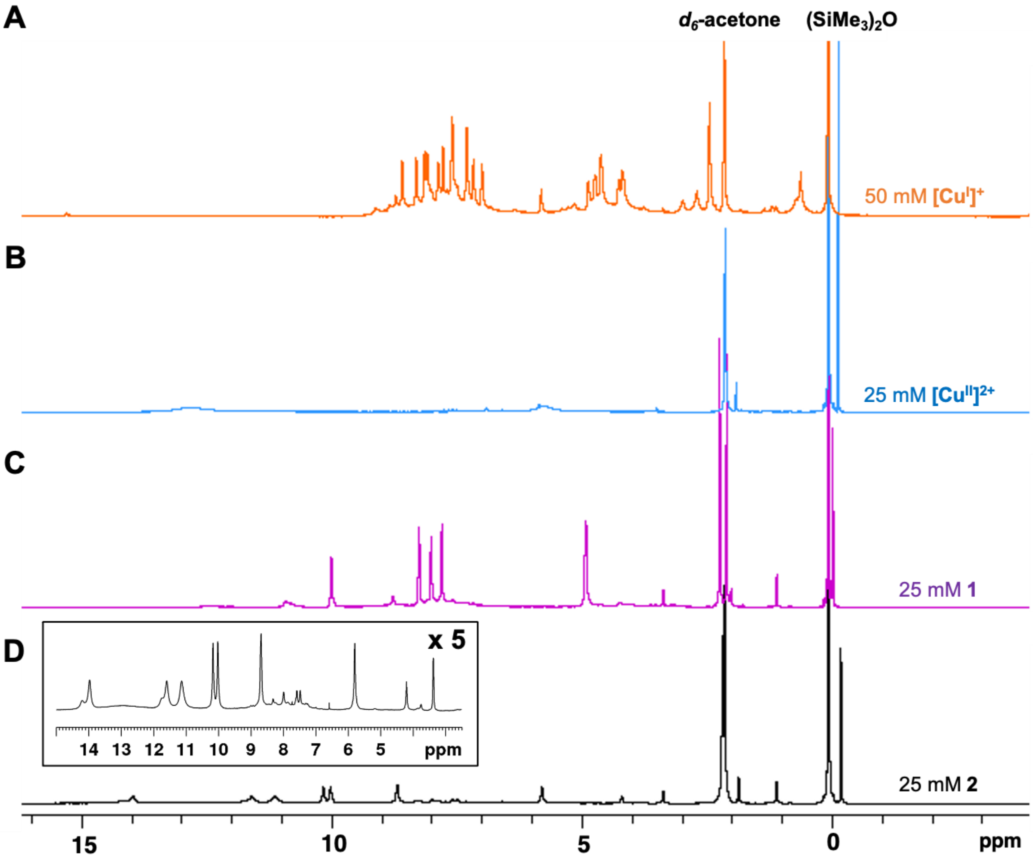

Figure S27. ^1H NMR spectra (d_6-acetone, 193 K) of **(A) $[Cu^I]^+$** (50 mM) + $Ca(OTf)_2$ (300 mM), **(B) $[Cu^{II}]^{2+}$** (25 mM) + $Ca(OTf)_2$ (300 mM), **(C) 1** (25 mM), **(D) 2** (25 mM) + $Ca(OTf)_2$ (300 mM). **Note:** spectra intensity was normalized to the internal standard, $(SiMe_3)_2O$ (5 mM).

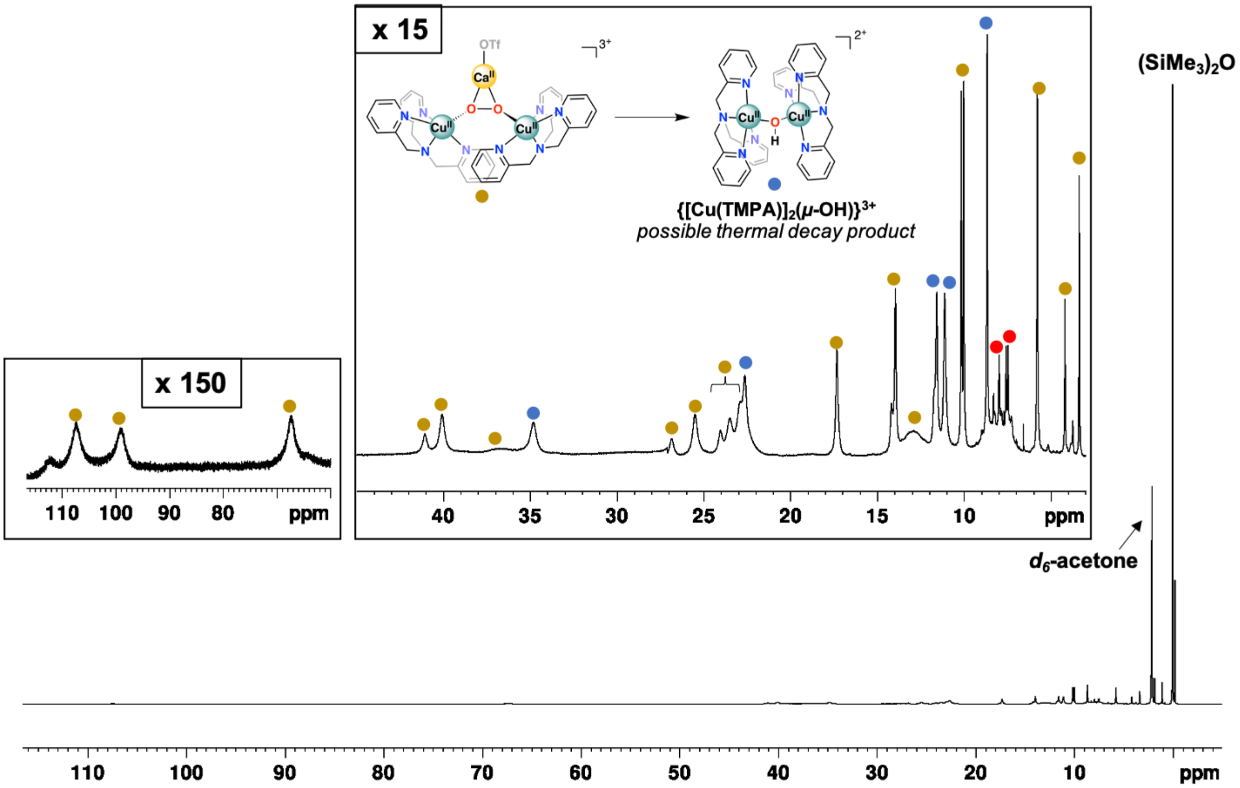

Figure S28. ^{1}H NMR (d_6-acetone, 193 K) of **2** (25 mM) + Ca(OTf)$_2$ (300 mM). Gold circles represent **2**. A small amount of diamagnetic impurity (red circles) was observed, along with a small amount of a thermal decomposition product (blue circles). As noted, **2** is otherwise stable at or below 193 K during our UV-Vis experiments, and thermal decomposition is likely due to any warming during sample transfer (only observed during NMR experiments). The ^{1}H-NMR resonances denoted with blue circles align with {[Cu^{II}(TMPA)]$_2$(μ-OH)}$^{3+}$ reported by Kieber-Emmons.[11, 16] **Note:** Integrations calibrated to (SiMe$_3$)$_2$O (5 mM) that was added as an internal standard in each sample. Insets show of 3-45 ppm and 50-115 ppm ranges; no peaks were observed below -4 ppm or above 120 ppm.

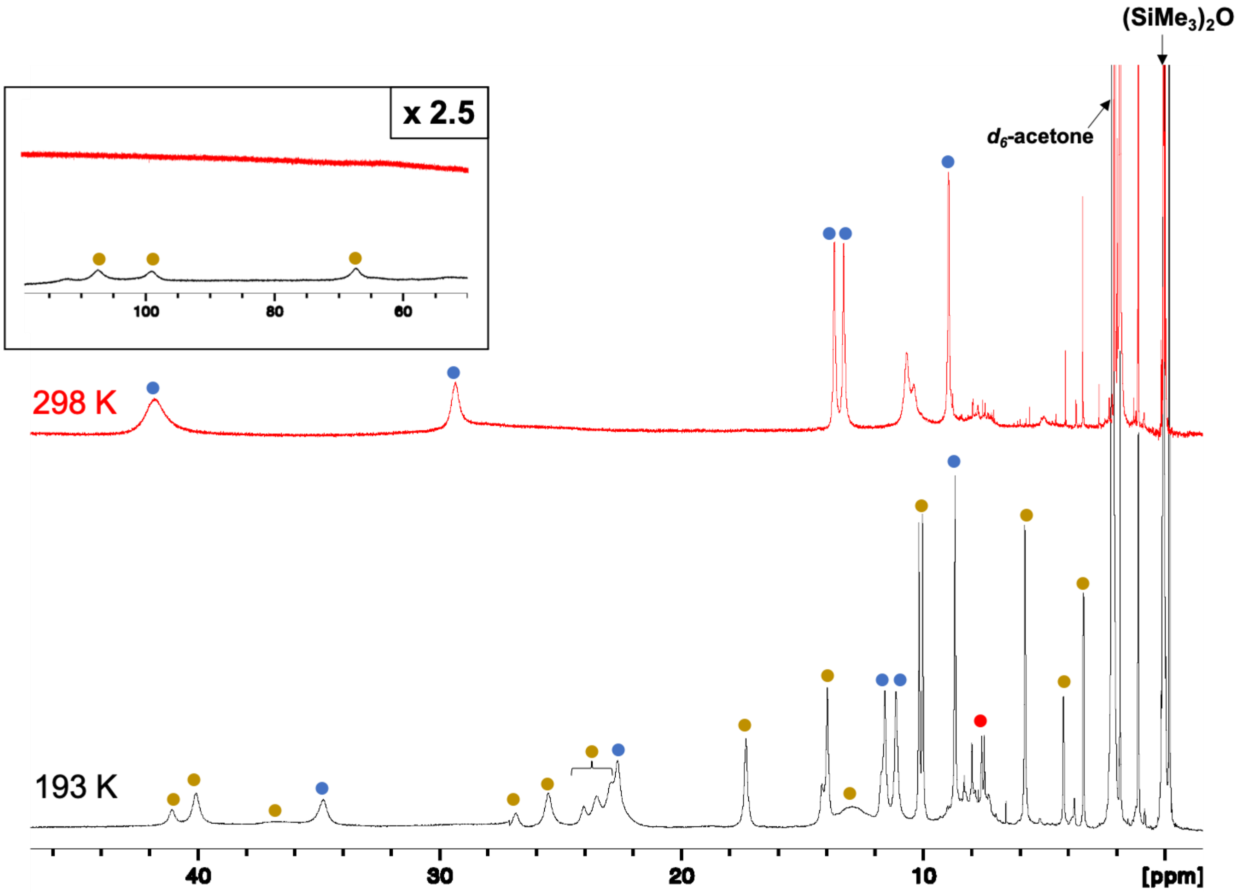

Figure S29. ^{1}H NMR (d_6-acetone) of of **2** (25 mM) + Ca(OTf)$_2$ (300 mM) starting at 193 K (bottom, black) and thermal decomposition product at 298 K (top, red) where inset represents downfield region from 50-120 ppm. Gold circles represent **2**, red circles represent small amount of diamagnetic substance and blue circles represent hypothesized decay product.[11, 16] **Note:** Peaks calibrated to (SiMe$_3$)$_2$O (5 mM) that was added as an internal standard.

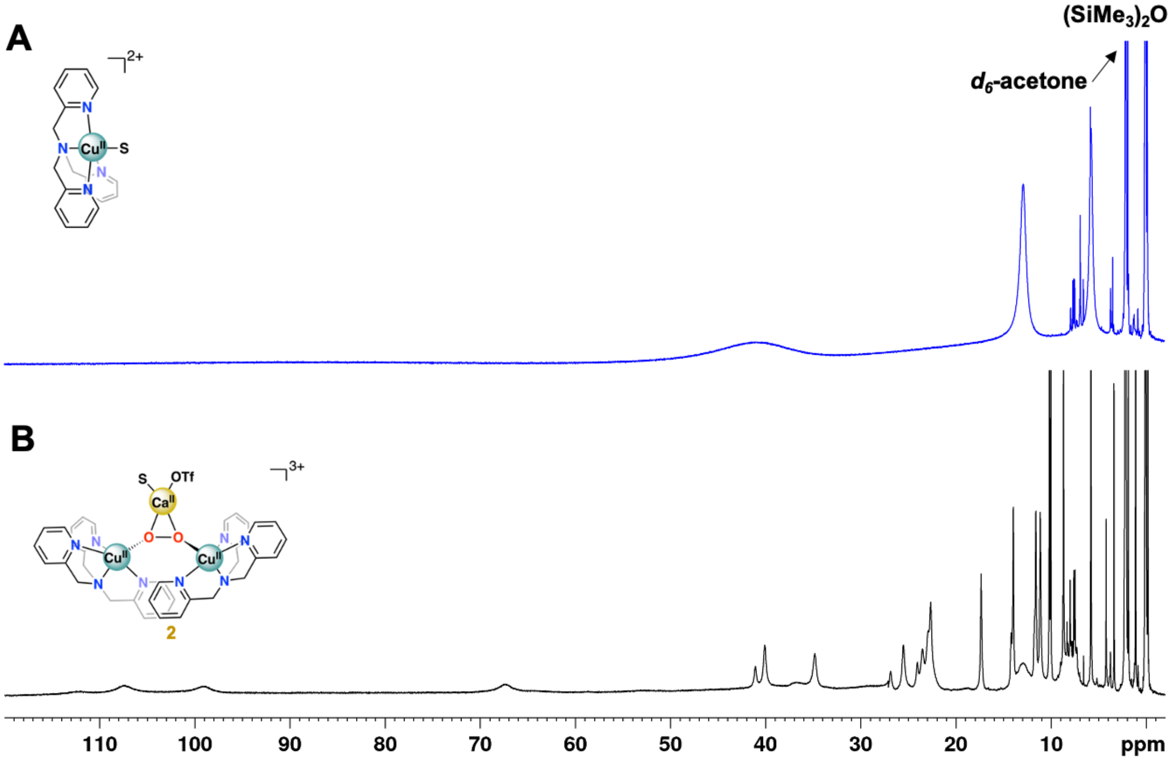

Figure S30. ^{1}H NMR (d_6-acetone, 193 K) of **(A) $[\mathrm{Cu^{II}}]^{2+}$** (25 mM) + $\mathrm{Ca(OTf)_2}$ (300 mM), **(B) 2** (25 mM) + $\mathrm{Ca(OTf)_2}$ (300 mM). **Note:** Peaks calibrated to the internal standard, $\mathrm{(SiMe_3)_2O}$ (5 mM).

6.3. Evans Method procedure

6.3.1. Procedure for determining effective magnetic moment

Evans Method measurements were taken using a Wilmad glass coaxial insert filled with 5 mM $(SiMe_3)_2O$ solution also used to prepare stock solutions for **$[Cu^I]^+$**, **$[Cu^{II}]^{2+}$**, **1** and **2**. The molar magnetic susceptibility, χ_{mol} ($cm^3 \cdot mol^{-1}$) and effective magnetic moment, μ_{eff} (μ_B, BM), were calculated using equations S11 and S12,[17] where Δf is the difference in Hz of the two observed $(SiMe_3)_2O$ peaks (Figure S31), f is the frequency of the NMR, C is concentration of solute ($mol \cdot cm^{-3}$), χ_D is the diamagnetic correction (see *6.2.2*) calculated from Pascal's constants ($cm^3 \cdot mol^{-1}$ or $emu \cdot mol^{-1}$), T is temperature (K), and n is the number of unpaired electrons.

$$\chi_{mol} = \frac{3\Delta f}{4\pi f C} - \chi_D \qquad \textbf{Eq. S11}$$

$$\mu_{eff} = \sqrt{8T\chi_{mol}} = \sqrt{n(n+2)} \qquad \textbf{Eq. S12}$$

6.3.2. Diamagnetic correction

Table S2. Pascal's constants[18] used to correct for the estimated diamagnetic susceptibility (χ_D) of solvent, ligand and metals present in each of the measured compounds.

Compound	**Pascal's Constants**		**χ_D (emu mol^{-1})**
Acetone			-33.6×10^{-6}
PF_6^-	χ_{Di}(P)	-26.3	-6.41×10^{-5}
	$6\chi_{Di}$(F)	6(-6.3)	
$CF_3SO_3^-$	χ_{Di}(C)	-6.0	-2.38×10^{-4}
	χ_{Di}(S)	-15.0	
	$3\chi_{Di}$(F)	3(-6.3)	
	$3\chi_{Di}$(O)	3(-4.6)	
TMPA	$15\chi_{Di}(C_{ring})$	15(-6.24)	-1.65×10^{-4}
	$3\chi_{Di}$(C)	3(-6.00)	
	$3\chi_{Di}(N_{ring})$	3(-4.61)	
	$1\chi_{Di}(N_{open\ chain})$	-5.57	
	$12\chi_{Di}$(H)	12(-2.93)	
	$3\chi_{Di}$(pyridine)	3(0.5)	
$[Cu^I]^+$	χ_D(TMPA)	-165	-2.09×10^{-4}
	$\chi_D(Cu^I)$	-12	
	$\chi_D(PF_6^-)$	-61.4	
$[Cu^{II}]^{2+}$	χ_D(TMPA)	-165	-2.40×10^{-4}
	$\chi_D(Cu^{II})$	-11	
	$2\chi_D(ClO_4^-)$	2(-32)	
1 [a]	$2\chi_D$(TMPA)	2(-165)	-4.84×10^{-4}
	$2\chi_D(Cu^{II})$	2(-11)	
	$2\chi_D(PF_6^-)$	2(-61.4)	
	$\chi_{Di}(O_2)$	2(-4.6)	
2 [a]	$2\chi_D$(TMPA)	2(-165)	-1.28×10^{-3}
	$2\chi_D(Cu^{II})$	2(-11)	
	$\chi_D(Ca^{II})$	-10.4	
	$2\chi_D(CF_3SO_3^-)$	2(-238.2)	
	$2\chi_D(PF_6^-)$	2(-64.1)	
	$\chi_{Di}(O_2)$	2(-4.6)	
	$2\chi_D$(Acetone)	3(-33.6)	

[a] χ_D of O_2 was used for O_2^{2-}; C-H and C-C single bonds assumed λ=0 emu mol^{-1}.

6.2.3. Effective Magnetic Moment Values

The μ_{eff} value of **[Cu$^{\mathrm{I}}$]$^+$** has been measured in MeCN at 233K as 0 BM.[19] Published μ_{eff} values of **1** vary depending on solvent ranging from 0.23 to 1.8 μ_B/Cu. Large values obtained for **1** were ascribed to paramagnetic impurities generated in CD_2Cl_2 measurement at 193K. Values of 0.23-0.33 μ_B/Cu were obtained in EtCN/C_7D_8 mixture at 193K where stability of **1** is improved in coordinating EtCN solvent.[3]

Table S3. $(SiMe_3)_2O$ frequency shift and μ_{eff} of Cu species obtained at 193K in d_6-acetone calculated using Evans method.

Entry	**Complex**	**Concentration (mM)**	**Δf (Hz)**	**μ_{eff} (μ_B)**	**μ_{eff} /Cu (μ_B/Cu)**
1[a]	**[Cu$^{\mathrm{I}}$]$^+$**	50	0	0	0
2[a]	**[Cu$^{\mathrm{II}}$]$^{2+}$**	25	117.391	1.80	1.80
3[b]	**[Cu$^{\mathrm{II}}$]$^{2+}$**	25	141.027	1.97	1.97
4	**1**	25	49.560	1.40	0.70
5[a,c]	**2**	25	149.969	2.44	1.22

a – Measured with 300 mM $Ca(OTf)_2$. *b* – No $Ca(OTf)_2$ added. *c* – Corrected for χ_{dia} associated with 300 mM $Ca(OTf)_2$ at 193 K (1.89 x 10^{-4} emu mol^{-1}; determined from differences in μ_{eff} of [Cu$^{\mathrm{II}}$]$^{2+}$ in entries 2 and 3).

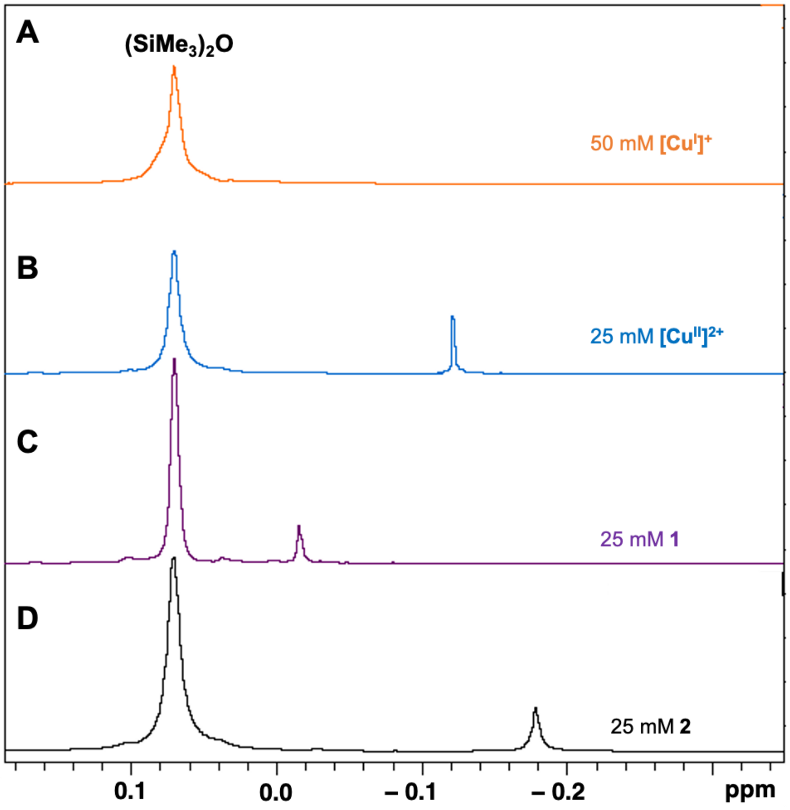

Figure S31. ^{1}H NMR (d_6-acetone, 193 K) of $(SiMe_3)_2O$ (5 mM) standard shifts used to calculate μ_{eff}: **(A) [Cu$^{\mathrm{I}}$]$^+$** (50 mM) + $Ca(OTf)_2$ (300 mM), **(B) [Cu$^{\mathrm{II}}$]$^{2+}$** (25 mM) + $Ca(OTf)_2$ (300 mM), **(C) 1** (25 mM), **(D) 2** (25 mM) + $Ca(OTf)_2$ (300 mM).

7. Conductivity Measurements

Conductivity measurements were performed using an Oakton Instruments CON 6+ meter with a conductivity/temperature probe that was calibrated according to the manufacturer specifications. Tetrabutyl ammonium triflate, [NBu$_4$][OTf], was used as a standard to represent formation of a 1:1 electrolyte in acetone (0.1 to 10 mM), where a molar conductivity (Λ_M) of 128 ± 10 S·cm^2/mol was obtained. This is consistent with quoted literature values of tetrabutyl ammonium salts in acetone (~10^{-3} M [NBu$_4$][Br]: 123 S·cm^2/mol).[20] The conductivity of Ca(OTf)$_2$ was measured in acetone (0.1 to 8 mM), and a molar conductivity of 107 ± 19 S·cm^2/mol was obtained. Although there is some deviation from ideal behavior at increasing concentrations of Ca(OTf)$_2$ (> 2 mM), the value of Λ_M still falls within the expected range of a 1:1 electrolyte (including Ca(ClO$_4$)$_2$ in acetone).[21] A reasonable formulation of this species would be [Ca(OTf)(Acetone)$_n$][OTf] ($n = 4$ or 5), and the reactivity of both [Ca(OTf)(Acetone)$_5$][OTf] and [Ca(OTf)$_2$(Acetone)$_4$] were explored in our computational modelling studies.

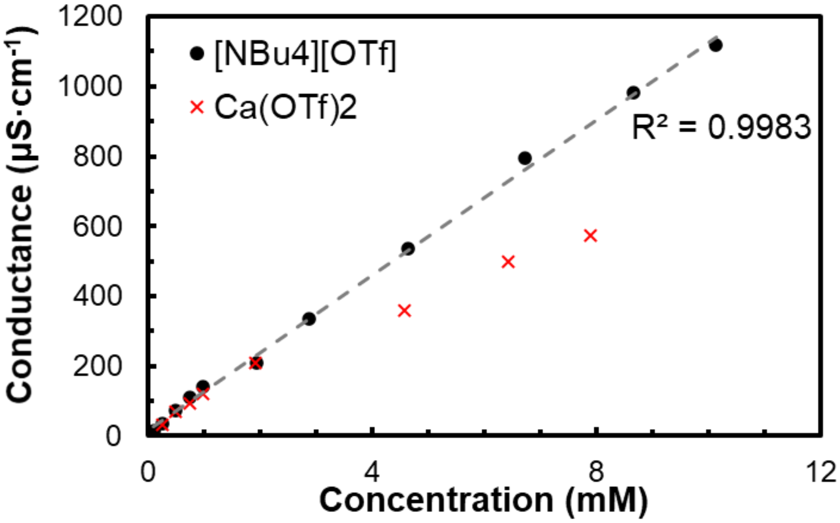

Figure S32. Conductivity measurements collected on acetone solutions at 298 K of [NBu$_4$][OTf] (black, ●) and Ca(OTf)$_2$ (red, ×).

9. Computational Methods

All geometries were fully optimized at the M06-L level of density functional theory[22] using the Stuttgart [8s7p6d2f | 6s5p3d2f] ECP10MWB contracted pseudopotential basis set on Cu[23] and the 6-31G(d) basis set[24] on all other atoms. The grid=ultrafine option in Gaussian 16[25] was chosen for integral evaluation and an automatically generated density-fitting basis set was used within the resolution-of-the-identity approximation for the evaluation of Coulomb integrals. The nature of all stationary points was verified by analytic computation of vibrational frequencies, which were also used for the computation of zero-point vibrational energies and molecular partition functions. Partition functions were used in the computation of 298 K thermal contributions to free energy employing the usual ideal-gas, rigid-rotator, harmonic oscillator approximation.[26] Solvation effects associated with acetone as solvent were accounted for by using the SMD continuum solvation model.[27] A 1 M standard state was used for all species in solution, thus, for all molecules, the free energy in solution is computed as the 1 atm gas-phase free energy, plus an adjustment for the 1 atm to 1 M standard-state concentration change of *RT* ln (24.5), or 1.9 kcal/mol, plus the 1 M to 1 M transfer (solvation) free energy computed from the SMD model.[26] Free energy contributions were added to single-point M06-L electronic energies computed with the SDD basis set on Cu and the 6-311+G(2df,p) basis set on all other atoms to arrive at final, composite free energies.

Many complexes investigated have electronic structures that are not well described by a single determinant. In such instances, standard Kohn-Sham DFT is not directly applicable,[26, 28] and we adopt the Yamaguchi broken-spin-symmetry (BS) procedure[29] to compute the energy of the spin-purified low-spin (LS) state as

$$^{\mathrm{LS}}E = \frac{^{\mathrm{BS}}E\left(^{\mathrm{HS}}\langle S^2\rangle - {}^{\mathrm{LS}}\langle S^2\rangle\right) - {}^{\mathrm{HS}}E\left(^{\mathrm{BS}}\langle S^2\rangle - {}^{\mathrm{LS}}\langle S^2\rangle\right)}{^{\mathrm{HS}}\langle S^2\rangle - {}^{\mathrm{BS}}\langle S^2\rangle} \qquad \textbf{(Eq. S13)}$$

where HS refers to the single-determinantal high-spin coupled state that is related to the low-spin state by spin flip(s) and $< S^2 >$ is the expectation value of the total spin operator applied to the appropriate determinant. The same procedure is employed to compute the exchange coupling constants (J) at B3LYP level of theory[30] with def2-TZVP basis set[31] on all atoms as implemented in ORCA software package.[32]

Figure S33. Optimized structures at M06-L level of theory. Color code: H, white; C, gray; N, blue; O, red; F, cyan; S, yellow; Ca, lime and Cu, ochre.

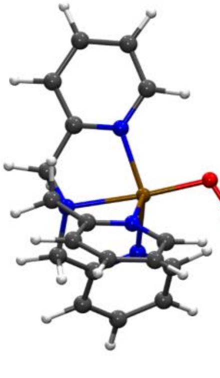 **{[Cu(TMPA)]$_2$(μ-1,2-O$_2$)}$^{2+}$**	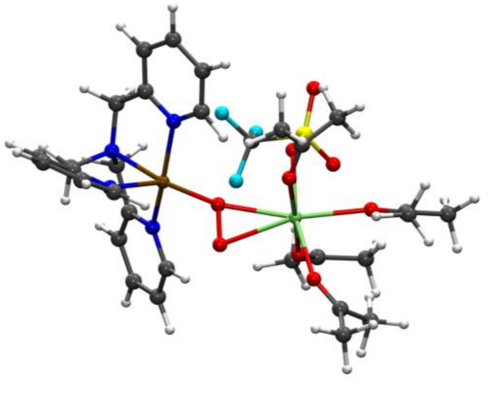 **{[Cu(TMPA)](μ-η^1:η^2:O$_2^{2-}$)[Ca(OTf)(Ac)$_4$]}$^{+}$ (A)**
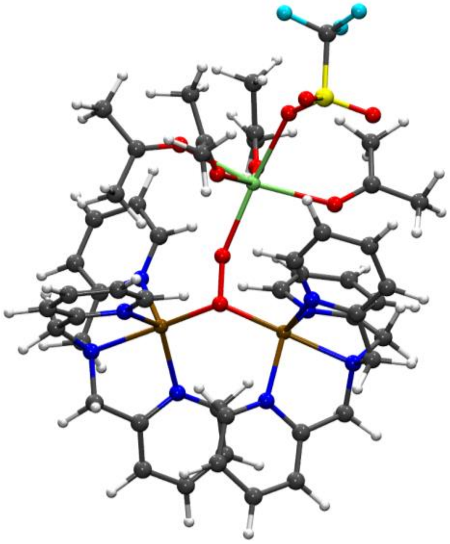 **{[Cu^{II}(TMPA)]$_2$(μ-η^1:η^1:η^1-O$_2^{2-}$)[Ca^{II}(OTf)(Ac)$_4$]}$^{3+}$ (B)** **Conformer 1**	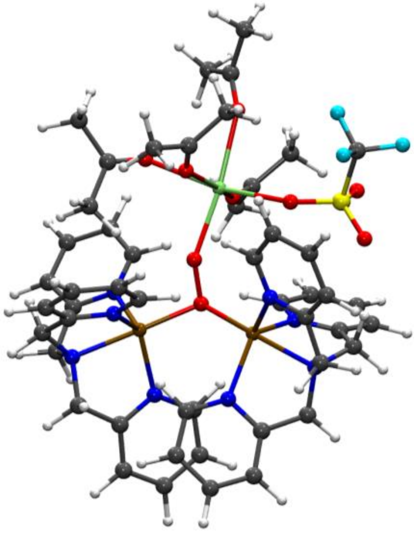 **{[Cu^{II}(TMPA)]$_2$(μ-η^1:η^1:η^1-O$_2^{2-}$)[Ca^{II}(OTf)(Ac)$_4$]}$^{3+}$ (B)** **Conformer 2**
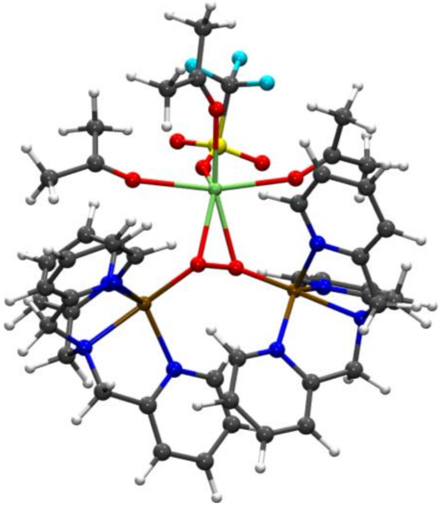	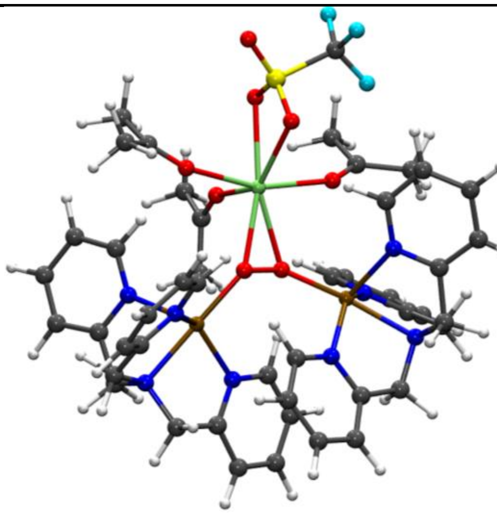

<table>
<tr><td>$\{[\mathrm{Cu^{II}(TMPA)}]_2(\mu\text{-}\eta^1\text{:}\eta^1\text{:}\eta^2\text{-}\mathrm{O_2}^{2-})[\mathrm{Ca^{II}(OTf)(Ac)_3}]\}^{3+}$
Conformer 1</td><td>$\{[\mathrm{Cu^{II}(TMPA)}]_2(\mu\text{-}\eta^1\text{:}\eta^1\text{:}\eta^2\text{-}\mathrm{O_2}^{2-})[\mathrm{Ca^{II}(OTf)(Ac)_3}]\}^{3+}$
Conformer 2</td></tr>
<tr><td colspan="2">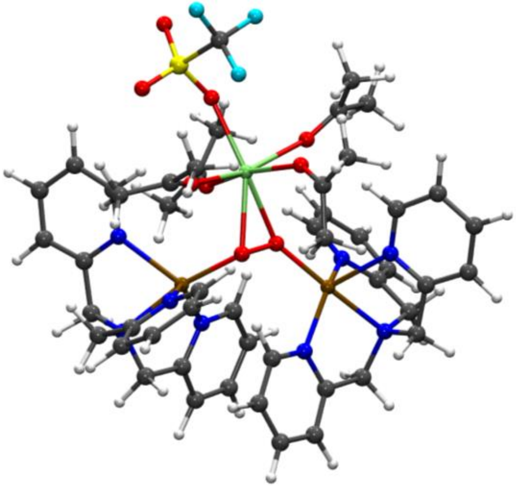
$\{[\mathrm{Cu^{II}(TMPA)}]_2(\mu\text{-}\eta^1\text{:}\eta^1\text{:}\eta^2\text{-}\mathrm{O_2}^{2-})[\mathrm{Ca^{II}(OTf)(Ac)_4}]\}^{3+}$ ($^{\mathrm{C}}$P)</td></tr>
</table>

Figure S34. Newman projections (and associated dihedral angles, φ) along the O – O bond for ^{C}**P** and the two conformers of the triacetone solvate, **{[Cu^{II}(TMPA)]$_2$(*μ*-*η*^{1}:*η*^{1}:*η*^{2}-O$_2$$^{2–}$)[Ca^{II}(OTf)(Ac)$_3$]}$^{3+}$.**

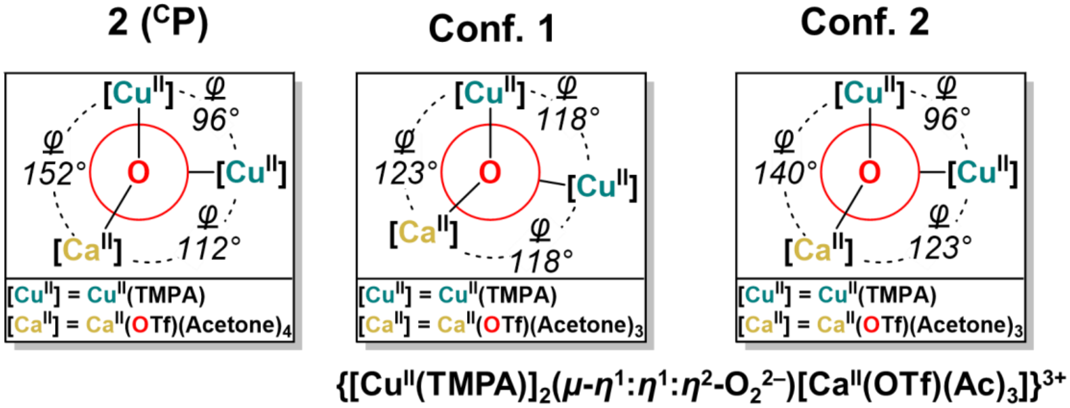

Figure S35. Unpaired spin density plots (blue and green surfaces indicate α and β spin densities respectively) for optimized structures at M06-L level of theory. Color code: H, omitted for clarity; C, gray; N, blue; O, red; F, cyan; S, yellow; Ca, lime and Cu, ochre.

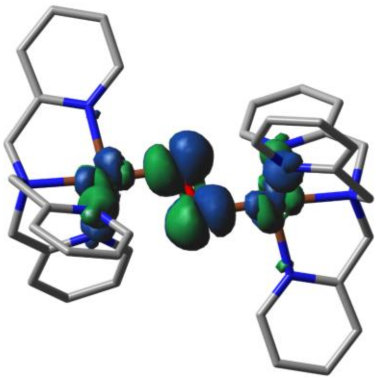 **{[Cu(TMPA)]$_2$(*μ*-1,2-O$_2$$^{2-}$)}$^{2+}$ (1)** **(S = 0)**	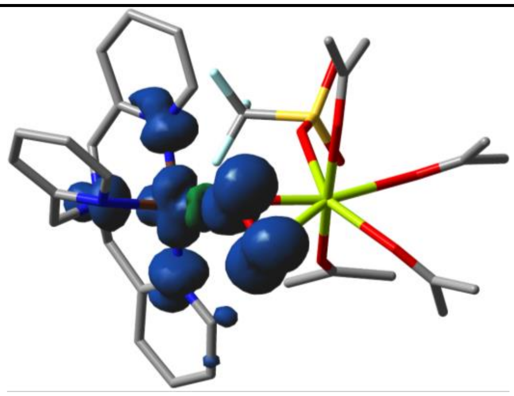 **{[Cu(TMPA)](*μ*-*η*^{1}:*η*^{2}:O$_2$$^{2-}$)[Ca(OTf)(Ac)$_4$]}$^+$ (A)** **(S = 1/2)**
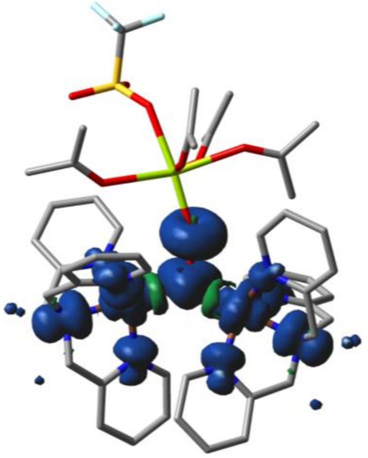 **{[Cu^{II}(TMPA)]$_2$(*μ*-*η*^{1}:*η*^{1}:*η*^{1}-O$_2$$^{2–}$)[Ca^{II}(OTf)(Ac)$_4$]}$^{3+}$ (B)** **Conformer 1 (*S* = 1, *J* = –36 cm^{-1})**	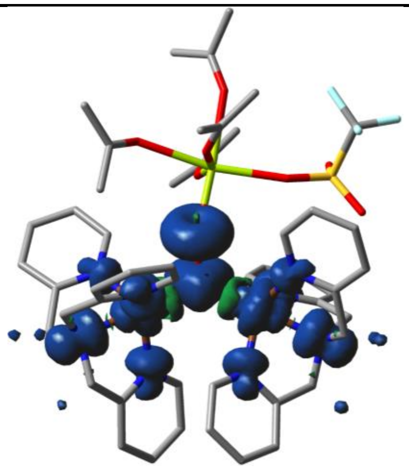 **{[Cu^{II}(TMPA)]$_2$(*μ*-*η*^{1}:*η*^{1}:*η*^{1}-O$_2$$^{2–}$)[Ca^{II}(OTf)(Ac)$_4$]}$^{3+}$ (B)** **Conformer 2 (*S* = 1, *J* = +11 cm^{-1})**

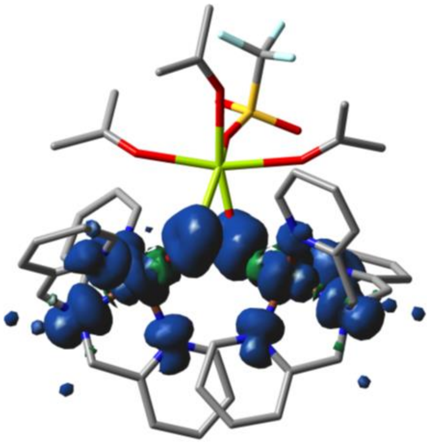

$\{[\mathrm{Cu^{II}(TMPA)}]_2(\mu\text{-}\eta^1{:}\eta^1{:}\eta^2\text{-}\mathrm{O_2^{2-}})[\mathrm{Ca^{II}(OTf)(Ac)_3}]\}^{3+}$
Conformer 1 (S = 1, J = –41 cm^{-1})

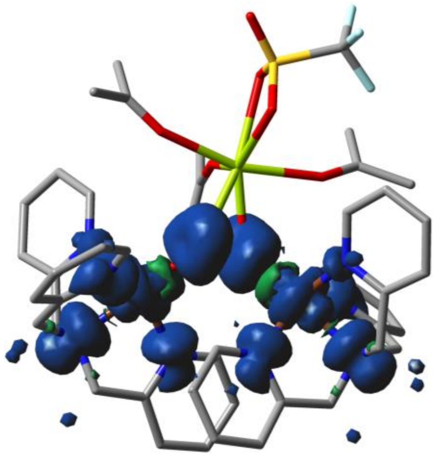

$\{[\mathrm{Cu^{II}(TMPA)}]_2(\mu\text{-}\eta^1{:}\eta^1{:}\eta^2\text{-}\mathrm{O_2^{2-}})[\mathrm{Ca^{II}(OTf)(Ac)_3}]\}^{3+}$
Conformer 2 (S = 1, J = +64 cm^{-1})

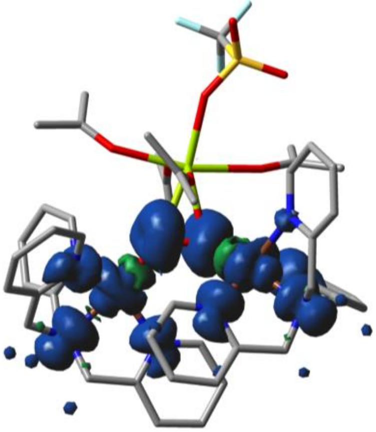

$\{[\mathrm{Cu^{II}(TMPA)}]_2(\mu\text{-}\eta^1{:}\eta^1{:}\eta^2\text{-}\mathrm{O_2^{2-}})[\mathrm{Ca^{II}(OTf)(Ac)_4}]\}^{3+}$ ($^{\mathrm{C}}$P)
(S = 1, J = +83 cm^{-1})

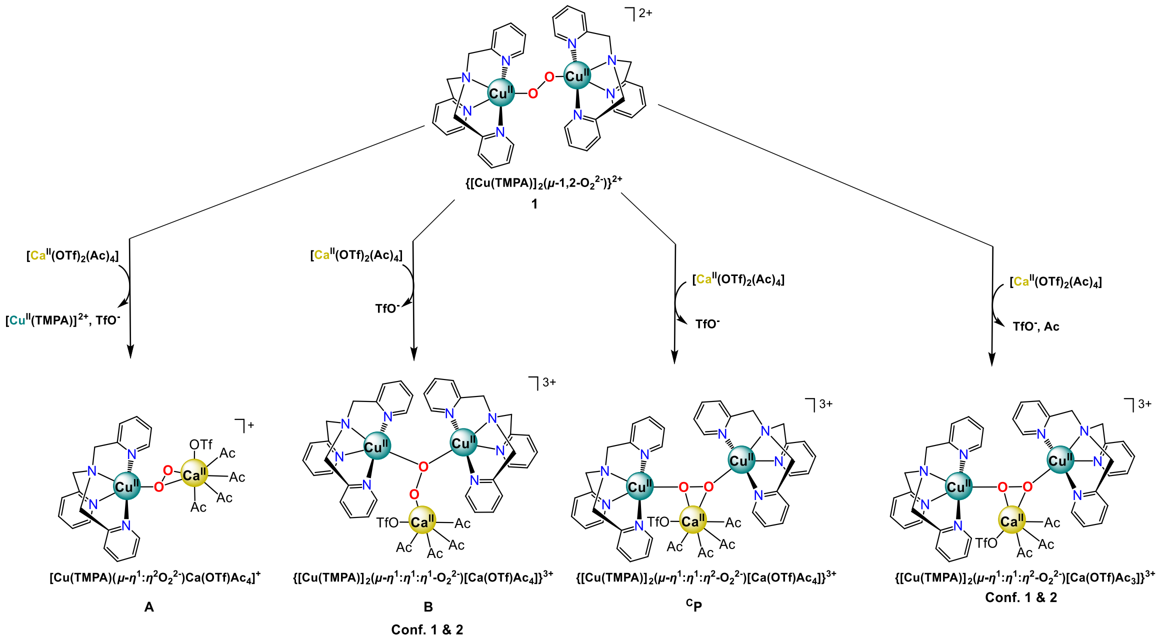

Compound	A	B		^{c}P	{[Cu(TMPA)]$_2$(μ-η^1:η^1:η^2-O$_2^{2-}$)[Ca(OTf)Ac$_3$]}$^{3+}$	
		(conf. 1)	(conf. 2)		(conf. 1, κ^1 OTf)	(conf. 2, κ^2 OTf)
ΔG (kcal/mol)	14.4	–0.8	–3.9	–9.6	–2.6	–9.1

Scheme S3. Computed free-energy changes (ΔG in kcal/mol) reactions of {**[Cu(TMPA)]$_2$(μ-1,2-O$_2$)]**}$^{2+}$ (**1**) and **[Ca(OTf)$_2$(Ac)$_4$]**

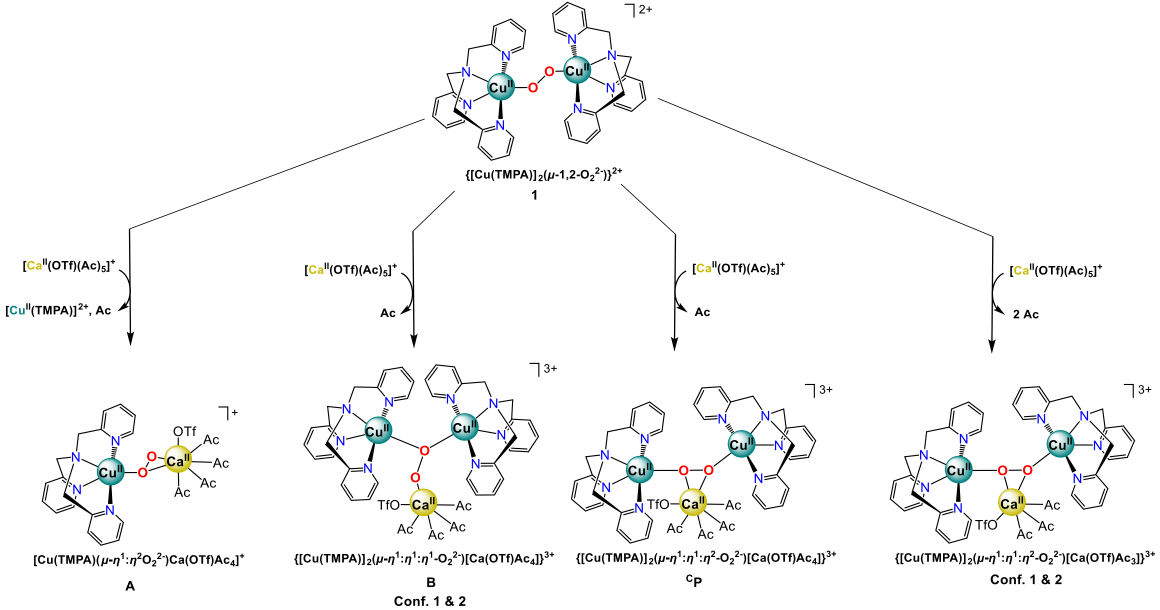

Compound	A	B		^{c}P	{[Cu(TMPA)]$_2$(μ-η^1:η^1:η^2-O$_2^{2-}$)[Ca(OTf)Ac$_3$]}$^{3+}$	
		(conf. 1)	(conf. 2)		(conf. 1, κ^1 OTf)	(conf. 2, κ^2 OTf)
ΔG (kcal/mol)	8.7	–6.5	–9.6	–15.3	–8.3	–14.8

Scheme S4. Computed free-energy changes (ΔG in kcal/mol) reactions of {**[Cu(TMPA)]$_2$(μ-1,2-O$_2$)]**}$^{2+}$ (**1**) and **[Ca(OTf)(Ac)$_5$]$^+$**

Table S4. Computed $\nu_{O–O}$ and $\Delta^{16}O_2–^{18}O_2$ in units of cm^{-1} for selected complexes.

Complex	Unscaled Frequencies		Scaled Frequencies scaling factor = 0.952	
	$\nu_{O–O}$	$\Delta^{16}O_2–^{18}O_2$	$\nu_{O–O}$	$\Delta^{16}O_2–^{18}O_2$
$\{[Cu^{II}(TMPA)]_2(\mu\text{-}\eta^1:\eta^1:\eta^1\text{-}O_2^{2-})[Ca^{II}(OTf)(Ac)_4]\}^{3+}$ Conformer 1 **(B)**	965	77	919	74
$\{[Cu^{II}(TMPA)]_2(\mu\text{-}\eta^1:\eta^1:\eta^1\text{-}O_2^{2-})\ [Ca^{II}(OTf)(Ac)_4]\}^{3+}$ Conformer 2 **(B)**	946	68	901	65
$\{[Cu^{II}(TMPA)]_2(\mu\text{-}\eta^1:\eta^1:\eta^2\text{-}O_2^{2-})[Ca^{II}(OTf)(Ac)_3]\}^{3+}$ **Conformer 1**	882	47	840	45
$\{[Cu^{II}(TMPA)]_2(\mu\text{-}\eta^1:\eta^1:\eta^2\text{-}O_2^{2-})[Ca^{II}(OTf)(Ac)_3]\}^{3+}$ **Conformer 2**	879	48	837	46
$\{[Cu^{II}(TMPA)]_2(\mu\text{-}\eta^1:\eta^1:\eta^2\text{-}O_2^{2})[Ca^{II}(OTf)(Ac)_4]\}^{3+}$ ^{C}**P**	873	48	831	45

9. Works Cited

(1) Kolthoff, I. M.; Chantooni, M. K.; Wang, W. J., Protonation and hydronium complexation stability constants of several crown ethers in acetonitrile. *Analytical Chemistry* **1983,** *55*, 1202-1204.

(2) Ramanaiah, K. V.; Ramkumar, V.; Murthy, N. N., High-spin iron(II) complexes of halides and pseudo-halides with biphenyl-appended N,N′-bidentate ligand: X-ray structural and spectroscopic studies. *Inorganica Chimica Acta* **2017,** *466*, 197-204.

(3) Tyeklar, Z.; Jacobson, R. R.; Wei, N.; Murthy, N. N.; Zubieta, J.; Karlin, K. D., Reversible reaction of dioxygen (and carbon monoxide) with a copper(I) complex. X-ray structures of relevant mononuclear Cu(I) precursor adducts and the trans-(.mu.-1,2-peroxo)dicopper(II) product. *Journal of the American Chemical Society* **1993,** *115*, 2677-2689.

(4) Wang, J.; Schopfer, M. P.; Puiu, S. C.; Sarjeant, A. A. N.; Karlin, K. D., Reductive Coupling of Nitrogen Monoxide (•NO) Facilitated by Heme/Copper Complexes. *Inorganic Chemistry* **2010,** *49*, 1404-1419.

(5) (a) Jacobson, R. R.; Tyeklar, Z.; Farooq, A.; Karlin, K. D.; Liu, S.; Zubieta, J., A copper-oxygen (Cu2-O2) complex. Crystal structure and characterization of a reversible dioxygen binding system. *Journal of the American Chemical Society* **1988,** *110*, 3690-3692. (b) Schatz, M.; Becker, M.; Thaler, F.; Hampel, F.; Schindler, S.; Jacobson, R. R.; Tyeklár, Z.; Murthy, N. N.; Ghosh, P.; Chen, Q.; Zubieta, J.; Karlin, K. D., Copper(I) Complexes, Copper(I)/O_2 Reactivity, and Copper(II) Complex Adducts, with a Series of Tetradentate Tripyridylalkylamine Tripodal Ligands $^{\triangledown}$. *Inorganic Chemistry* **2001,** *40*, 2312-2322. (c) Zhang, C. X.; Kaderli, S.; Costas, M.; Kim, E.-i.; Neuhold, Y.-M.; Karlin, K. D.; Zuberbühler, A. D., Copper(I)−Dioxygen Reactivity of $[(L)Cu^{I}]^{+}$ (L = Tris(2-pyridylmethyl)amine): Kinetic/Thermodynamic and Spectroscopic Studies Concerning the Formation of $Cu-O_2$ and Cu_2-O_2 Adducts as a Function of Solvent Medium and 4-Pyridyl Ligand Substituent Variations. *Inorganic Chemistry* **2003,** *42*, 1807-1824.

(6) (a) Park, Y. S.; Paek, K., Hydrazide as a New Hydrogen-Bonding Motif for Resorcin[4]arene-Based Molecular Capsules. *Organic Letters* **2008,** *10*, 4867-4870. (b) SDBSWeb https://sdbs.db.aist.go.jp/sdbs/cgi-bin/landingpage?sdbsno=15709 (accessed 8/28/2020).

(7) Jacobson, R. R.; Tyeklar, Z.; Karlin, K. D.; Zubieta, J., Fluoride as a terminal and bridging ligand for copper: isolation and x-ray crystallographic characterization of copper monomeric and dimeric complexes [CuII(TMPA)F]nn+ (n = 1 or 2; TMPA = tris[(2-pyridyl)methyl]amine). *Inorganic Chemistry* **1991,** *30*, 2035-2040.

(8) Thordarson, P., Determining association constants from titration experiments in supramolecular chemistry. *Chem. Soc. Rev.* **2011,** *40*, 1305-1323.

(9) Espenson, J. H., *Chemical kinetics and reaction mechanisms*. Citeseer: 1995; Vol. 102.

(10) Fry, H. C.; Scaltrito, D. V.; Karlin, K. D.; Meyer, G. J., The Rate of O_2 and CO Binding to a Copper Complex, Determined by a "Flash-and-Trap" Technique, Exceeds that for Hemes. *Journal of the American Chemical Society* **2003,** *125*, 11866-11871.

(11) Ali, G.; VanNatta, P. E.; Ramirez, D. A.; Light, K. M.; Kieber-Emmons, M. T., Thermodynamics of a μ-oxo Dicopper(II) Complex for Hydrogen Atom Abstraction. *Journal of the American Chemical Society* **2017,** *139*, 18448-18451.

(12) Kakuda, S.; Peterson, R. L.; Ohkubo, K.; Karlin, K. D.; Fukuzumi, S., Enhanced Catalytic Four-Electron Dioxygen (O_2) and Two-Electron Hydrogen Peroxide (H_2O_2) Reduction with a Copper(II) Complex Possessing a Pendant Ligand Pivalamido Group. *Journal of the American Chemical Society* **2013,** *135*, 6513-6522.

(13) Drago, R. S., *Physical methods for chemists*. 1992.

(14) Kakuda, S.; Rolle, C. J.; Ohkubo, K.; Siegler, M. A.; Karlin, K. D.; Fukuzumi, S., Lewis Acid-Induced Change from Four- to Two-Electron Reduction of Dioxygen Catalyzed by Copper Complexes Using Scandium Triflate. *Journal of the American Chemical Society* **2015,** *137*, 3330-3337.

(15) Lee, D.-H.; Wei, N.; Murthy, N. N.; Tyeklar, Z.; Karlin, K. D.; Kaderli, S.; Jung, B.; Zuberbuehler, A. D., Reversible O2 Binding to a Dinuclear Copper(I) Complex with Linked Tris(2-pyridylmethyl)amine Units: Kinetic-Thermodynamic Comparisons with Mononuclear Analogs. *Journal of the American Chemical Society* **1995,** *117*, 12498-12513.

(16) VanNatta, P. E.; Ramirez, D. A.; Velarde, A. R.; Ali, G.; Kieber-Emmons, M. T., Exceptionally High O–H Bond Dissociation Free Energy of a Dicopper(II) μ-Hydroxo Complex and Insights into the Geometric and Electronic Structure Origins Thereof. *Journal of the American Chemical Society* **2020**, jacs.0c06425.

(17) Evans, D. F., 400. The determination of the paramagnetic susceptibility of substances in solution by nuclear magnetic resonance. *Journal of the Chemical Society (Resumed)* **1959**, 2003-2005.

(18) Bain, G. A.; Berry, J. F., Diamagnetic Corrections and Pascal's Constants. *Journal of Chemical Education* **2008,** *85*, 532.

(19) Ghiladi, R. A.; Chufán, E. E.; del Río, D.; Solomon, E. I.; Krebs, C.; Huynh, B. H.; Huang, H.-w.; Moënne-Loccoz, P.; Kaderli, S.; Honecker, M.; Zuberbühler, A. D.; Marzilli, L.; Cotter, R. J.; Karlin, K. D., Further Insights into the Spectroscopic Properties, Electronic Structure, and Kinetics of Formation of the Heme−Peroxo−Copper Complex [(F8TPP)FeIII−(O22-)−CuII(TMPA)]+. *Inorganic Chemistry* **2007,** *46*, 3889-3902.

(20) (a) Geary, W. J., The use of conductivity measurements in organic solvents for the characterisation of coordination compounds. *Coordination Chemistry Reviews* **1971,** *7*, 81-122. (b) Huttemann, T. J.; Foxman, B. M.; Sperati, C. R.; Verkade, J. G., Transition Metal Complexes of a Constrained Phosphite Ester. IV. Compounds of Cobalt(I), Cobalt(III), Nickel(II), and Nickel(0). *Inorganic Chemistry* **1965,** *4*, 950-953.

(21) Rysselberghe, P. V.; Fristrom, R. M., The Conductance of Non-aqueous Solutions of Magnesium and Calcium Perchlorates1. *Journal of the American Chemical Society* **1945,** *67*, 680-682.

(22) Zhao, Y.; Truhlar, D. G., A new local density functional for main-group thermochemistry, transition metal bonding, thermochemical kinetics, and noncovalent interactions. *The Journal of Chemical Physics* **2006,** *125*, 194101.

(23) Dolg, M.; Wedig, U.; Stoll, H.; Preuss, H., Energy-adjusted ab initio pseudopotentials for the first row transition elements. *The Journal of Chemical Physics* **1987,** *86*, 866-872.

(24) Hehre, W. J. R., Leo; Schleyer, Paul von R.; Pople, John A., *Ab Initio Molecular Orbital Theory*. Wiley: New York, 1986.

(25) Frisch, M. J. T., G. W.; Schlegel, H. B.; Scuseria, G. E.; Robb, M. A.; Cheeseman, J. R.; Scalmani, G.; Barone, V.; Petersson, G. A.; Nakatsuji, H.; Li, X.; Caricato, M.; Marenich, A. V.; Bloino, J.; Janesko, B. G.; Gomperts, R.; Mennucci, B.; Hratchian, H. P.; Ortiz, J. V.; Izmaylov, A. F.; Sonnenberg,

J. L.; Williams-Young, D.; Ding, F.; Lipparini, F.; Egidi, F.; Goings, J.; Peng, B.; Petrone, A.; Henderson, T.; Ranasinghe, D.; Zakrzewski, V. G.; Gao, J.; Rega, N.; Zheng, G.; Liang, W.; Hada, M.; Ehara, M.; Toyota, K.; Fukuda, R.; Hasegawa, J.; Ishida, M.; Nakajima, T.; Honda, Y.; Kitao, O.; Nakai, H.; Vreven, T.; Throssell, K.; Montgomery, J. A., Jr.; Peralta, J. E.; Ogliaro, F.; Bearpark, M. J.; Heyd, J. J.; Brothers, E. N.; Kudin, K. N.; Staroverov, V. N.; Keith, T. A.; Kobayashi, R.; Normand, J.; Raghavachari, K.; Rendell, A. P.; Burant, J. C.; Iyengar, S. S.; Tomasi, J.; Cossi, M.; Millam, J. M.; Klene, M.; Adamo, C.; Cammi, R.; Ochterski, J. W.; Martin, R. L.; Morokuma, K.; Farkas, O.; Foresman, J. B.; Fox, D. J. *Gaussian 16*, Gaussian, Inc.: Wallingford CT, 2016.
(26) Cramer, C. J., *Essentials of Computational Chemistry: Theories and Models*. 2nd Edition ed.; John Wiley & Sons Ltd: Chichester, 2004.
(27) Marenich, A. V.; Cramer, C. J.; Truhlar, D. G., Universal Solvation Model Based on Solute Electron Density and on a Continuum Model of the Solvent Defined by the Bulk Dielectric Constant and Atomic Surface Tensions. *The Journal of Physical Chemistry B* **2009,** *113*, 6378-6396.
(28) (a) Ziegler, T.; Rauk, A.; Baerends, E. J., On the calculation of multiplet energies by the hartree-fock-slater method. *Theoretica chimica acta* **1977,** *43*, 261-271. (b) Noodleman, L., Valence bond description of antiferromagnetic coupling in transition metal dimers. *The Journal of Chemical Physics* **1981,** *74*, 5737-5743. (c) Cramer, C. J.; Truhlar, D. G., Density functional theory for transition metals and transition metal chemistry. *Physical Chemistry Chemical Physics* **2009,** *11*, 10757-10816.
(29) (a) Yamaguchi, K.; Jensen, F.; Dorigo, A.; Houk, K. N., A spin correction procedure for unrestricted Hartree-Fock and Møller-Plesset wavefunctions for singlet diradicals and polyradicals. *Chemical Physics Letters* **1988,** *149*, 537-542. (b) Soda, T.; Kitagawa, Y.; Onishi, T.; Takano, Y.; Shigeta, Y.; Nagao, H.; Yoshioka, Y.; Yamaguchi, K., Ab initio computations of effective exchange integrals for H-H, H-He-H and Mn ₂O ₂ complex: comparison of broken-symmetry approaches. *Chemical Physics Letters* **2000,** *319*, 223-230.
(30) Becke, A. D., Density-functional thermochemistry. III. The role of exact exchange. *The Journal of Chemical Physics* **1993,** *98*, 5648-5652.
(31) Weigend, F.; Ahlrichs, R., Balanced basis sets of split valence, triple zeta valence and quadruple zeta valence quality for H to Rn: Design and assessment of accuracy. *Physical Chemistry Chemical Physics* **2005,** *7*, 3297-3305.
(32) Neese, F.; Wennmohs, F.; Becker, U.; Riplinger, C., The ORCA quantum chemistry program package. *The Journal of Chemical Physics* **2020,** *152*, 224108.